Université de Montréal

Étude des mécanismes d'ablation laser par impulsions ultra-courtes à l'aide de la dynamique moléculaire

par
Danny Perez

Département de Physique
Faculté des arts et des sciences

Mémoire présenté à la Faculté des études supérieures
en vue de l'obtention du grade de Maître ès sciences (M.Sc.)
en Physique

Octobre, 2002

Université de Montréal
Faculté des études supérieures

Ce mémoire intitulé:

Étude des mécanismes d'ablation laser par impulsions ultra-courtes à l'aide de la dynamique moléculaire

présenté par:

Danny Perez

a été évalué par un jury composé des personnes suivantes:

Michel Meunier,	président-rapporteur
Laurent J. Lewis ,	directeur de recherche
Sjoerd Roorda,	membre du jury

Mémoire accepté le: .....

RÉSUMÉ

Une étude des mécanismes d'ablation laser par impulsions ultra-courtes à été réalisée au moyen de la dynamique moléculaire. Les simulations ont été effectuées à l'aide d'un modèle simple composé d'atomes interagissant par un potentiel de Lennard-Jones dans un espace bidimensionnel. L'impulsion laser, d'une longueur de 100 fs, excite un gaz de porteurs qui relaxent ensuite en transférant leur énergie au réseau. Pour des énergies suffisamment élevées, ce chauffage intense cause l'éjection d'atomes de la surface de la cible, un processus nommé ablation. Les conditions dans lesquelles l'ablation survient ont tout d'abord été déterminées par une étude de la dynamique d'expansion de la cible et de la génération d'ondes de pression durant la relaxation. Les résultats démontrent l'existence de plusieurs régimes d'expansion distincts selon l'énergie localement absorbée dans la cible. L'origine de ces différents régimes est liée à des variations importantes dans la forme des isentropes le long desquelles la relaxation s'effectue à mesure que l'énergie absorbée augmente. Les ondes de pression générées subissent aussi des changements majeurs avec l'augmentation de la fluence : les profils d'onde passent de bipolaires à unipolaires suite à la perte de résistance tensile du matérial à haute température. En combinant les données sur les régimes d'expansion et sur les ondes acoustiques avec une analyse de l'évolution thermodynamique du système, les mécanismes responsables de l'ablation de matière sont ensuite identifiés. Les simulations démontrent que quatre mécanismes peuvent être responsables de l'ablation par impulsions femtoseconde sous le seuil de formation de plasma : la spallation sous l'effet de l'onde tensile, l'explosion de phase, la fragmentation photo-mécanique (identifiée ici pour la première fois dans un contexte d'ablation laser) et la vaporisation. Ces mécanismes peuvent être actifs simultanément à différentes profondeurs dans la cible. Les résultats du modèle sont en accord avec plusieurs mesures expérimentales.

Mots clés : ablation laser, impulsions ultra-courtes, simulations numériques

ABSTRACT

A molecular-dynamics study of the mechanisms of ablation by ultrashort laser pulses has been performed. Simulations where carried out using a simple two-dimensional Lennard-Jones model. A 100 fs long laser pulse is used to excite a carrier gas which then relaxes gradually by transferring energy to the lattice. If the injected energy is large enough, ejection of atoms from the surface of the target occurs ; this process is called ablation. Conditions in which ablation occurs are first investigated. Results show that different expansion regimes are present depending on the shape of the isentropes along which relaxation occurs. The pressure waves generated during the early part of the relaxation also suffer some changes as the fluence is increased : the low-fluence bipolar profile becomes unipolar as a result of the reduced tensile strength of the material at high temperature. Coupling the results of this first part of the investigation with the analysis of the thermodynamical evolution of the system, the mechanisms responsible for ablation are identified. Simulations show that four mechanisms induce ablation under the threshold for plasma formation : spallation as a result of the passage of a tensile wave, phase explosion, photo-mechanical fragmentation and vaporization. These mechanisms can be active at the same time to induce ablation of the material at different depths under the surface of the target. Results of the model are in good agreement with experiments.

Key words : laser ablation, ultra-short pulses, numérical simulations

TABLE DES MATIÈRES

LISTE DES FIGURES

LISTE DES ANNEXES

LISTE DES NOTATIONS ET DES SYMBOLES

DM : Dynamique Moléculaire

ICP-MS : *Inductively coupled plasma—mass spectrometry*

LJ : Lennard-Jones

PLD : *Pulsed Laser Deposition*

REMERCIEMENTS

Plusieur personnes m'ont assisté directement ou indirectement durant ces deux années de travail. J'aimerais adresser un merci particulier à mon directeur de recherche, Laurent J. Lewis, pour sa disponibilité malgré son emploi du temps plus que chargé, ses judicieux conseils à toutes les étapes de ce projet ainsi que pour sa bonne humeur et son humour légendaire. Je dois aussi une fière chandelle à mon collègue Patrick Lorazo. Nos discussions m'ont permis d'approfondir mes connaissances sur le sujet et de tester mes idées. Merci aussi aux professeurs et étudiants du groupe (Michel, Normand, Colin, Cristiano, Ralf, Pierre C., Pierre T., Anna, Jean-Charles, Fedwa, Nassima, Jean-François et Philippe) grâce à qui l'ambiance de travail au bureau fut fort agréable et productive. J'aimerais aussi souligner le travail exceptionnel de tous les responsables des ressources informatiques, notamment Bernard Lorazo, Jacques Richer et Yves Léger.

Sur une note plus personnelle, j'aimerais remercier ma famille et plus particulièrement ma mère qui m'a toujours soutenu tout au long de mes études. Finalement, merci à mes amis Carl, Yannick, François et Stéphane pour le doux délire dans lequel ils m'ont plongé durant toutes ces années en leur compagnie.

INTRODUCTION

0.1 Ablation laser

L'ablation laser est le processus par lequel de la matière est éjectée de la surface d'un échantillon suite à l'irradiation de celui-ci par un faiseau laser. La matière peut être éjectée sous plusieurs formes : fragments solides, gouttelettes liquides, atomes isolés ou encore, comme c'est le plus souvent le cas, sous la forme d'un mélange de ces différentes phases. Bien que l'ablation laser puisse se produire avec des impulsions de toute durée (et même avec des lasers à fonctionnement continu), l'utilisation d'impulsions ultra-courtes (d'une durée comprise entre la nano et la femtoseconde) est particulièrement intéressante pour de nombreuses applications technologiques de pointe.

0.2 Intérêt technologique de l'ablation laser par impulsions ultra-courtes

L'intérêt initialement porté à l'ablation laser par impulsions ultra-courtes provient principalement de son application au dépôt de couches minces (technique dite *pulsed laser deposition* ou PLD) [60]. Comme le montre la figure 1, le principe de

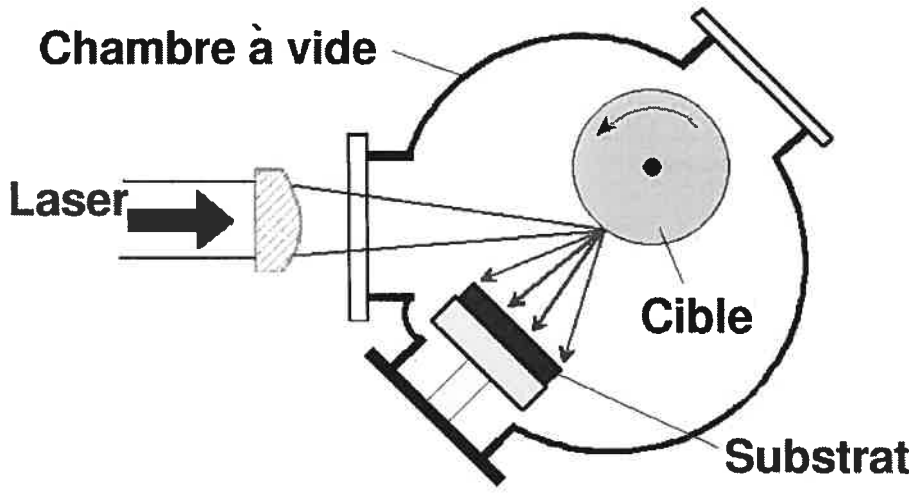

FIG. 1 – Représentation schématique d'un montage de PLD.

fonctionnement de la PLD est très simple. Un échantillon du matériel que l'on sou-

haite déposer est d'abord placé à l'intérieur d'une chambre à vide ; cet échantillon est nommé cible. Après avoir introduit un gaz dans l'enceinte ou après y avoir fait le vide, on illumine la cible à l'aide d'impulsions laser intenses. Le matériel éjecté de la cible est alors propulsé vers le substrat sur lequel il se dépose, formant graduellement une couche mince sur sa surface. Le nombre d'impulsions incidentes sur la cible est ajusté de manière à obtenir l'épaisseur de film voulue. L'avantage de la PLD sur les autres techniques de déposition vient du fait qu'elle permet le dépôt efficace de couches minces de matériaux à stoechiométrie complexe (tels les supraconducteurs à haute température critique par exemple). Bien que l'enthousiasme soulevé par la mise au point de cette technique se soit quelque peu estompé lorsque la difficulté d'application de la PLD à grande échelle est devenue évidente, le dépôt de couches minces par ablation laser reste une technique de choix pour les applications de recherche et de développement car sa simplicité et sa polyvalence permettent la synthèse efficace d'une grande variété de composés. La PLD permet aussi la fabrication de films aux propriétés uniques (composés de matériaux nanocristallins par exemple), hors de la portée des autres méthodes de croissance.

Depuis son application à la PLD, l'ablation laser par impulsions ultra-courtes a fait son apparition dans de nombreux autres domaines d'application. Par exemple, une technique d'analyse chimique (nommée "Inductively coupled plasma—mass spectrometry" ou ICP-MS) tire aussi profit du processus d'ablation laser. Dans ce cas, l'échantillon est introduit à l'intérieur d'un plasma, ce qui a pour effet de dissocier les molécules et d'ioniser une partie des atomes présents. Ce plasma est ensuite dirigé vers un spectromètre de masse, lequel détermine de manière précise (moins de une partie par milliard de résolution) le contenu de l'échantillon. À l'origine, les échantillons étudiés devaient être mis en solution avant d'être introduits dans le plasma. Depuis peu, on utilise plutôt l'ablation laser pour vaporiser une partie de l'échantillon et pour diriger le matériel éjecté à l'intérieur du plasma (voir figure 2 et Ref. [6] par exemple). Ceci permet d'éviter le long processus de mise en solution ainsi que la contamination de l'échantillon qui survenait fréquemment durant cette étape. Les chercheurs ont constaté que l'utilisation d'impulsions ultra-courtes permet d'obtenir des résultats plus reproductibles (éjection d'une quantité de masse

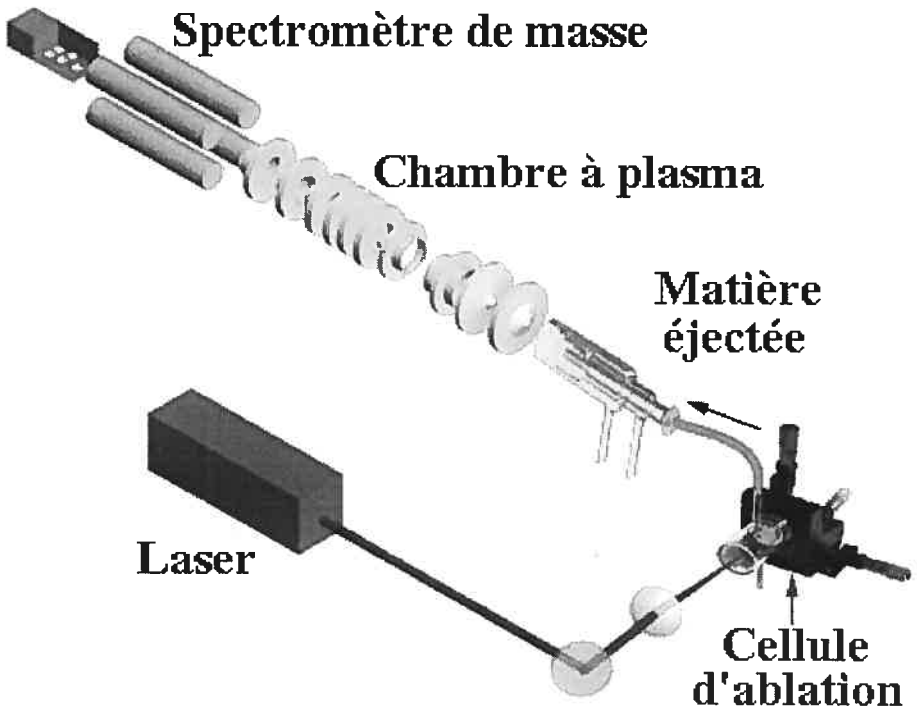

FIG. 2 – Représentation schématique d'un montage de ICP-MS ("Inductively coupled plasma—mass spectrometry") laser. Image tirée du site : `http ://teamd.lbl.gov/`

constante d'impulsion en impulsion) qu'avec les impulsion plus longues.

L'ablation laser est aussi un outil indispensable dans beaucoup d'autres champs d'étude : micro-usinage [67], ophtalmologie [38] et dentisterie, [42] pour n'en citer que quelques-uns. À la lumière de l'importante quantité d'applications qui tirent profit de cette technique, il est évident qu'une compréhension poussée des mécanismes qui causent l'ablation permettrait d'optimiser plusieurs de ces procédés.

0.3 Mécanismes d'ablation

Une connaissance profonde des mécanismes d'ablation et de leurs caractéristiques permettrait de déterminer les paramètres optimaux pour une application donnée. Par exemple, pour être efficace, la PLD requiert un contrôle précis de la distribution en taille, en vitesse et en température des amas éjectés de la cible sous différentes conditions. Les application ICP-MS requièrent, quant a elles, une connaissance précise de la quantité de matériel éjecté à chaque impulsion, variable

essentielle à la détermination adéquate des diverses concentrations en espèces chimiques. Les application en micro-usinage exigent aussi un fin contrôle de la quantité de matière éjectée ainsi que des dommages thermiques et mécaniques subis par le substrat usiné. C'est ce constat qui a motivé l'orientation de nos recherches vers l'identification des mécanismes susceptibles de causer l'ablation. Devant la formidable complexité des différents processus d'interaction laser-matière (variation des propriétés optiques et électroniques de la cible, fusion non-thermique, transition semiconducteur-métal, formation de plasma, etc), nous avons choisi de nous concentrer sur l'identification des mécanismes mésoscopiques qui donnent lieu à l'éjection de quantités importantes de matière. Même à ce niveau, la tâche reste très complexe.

Bien que plusieurs processus aient été proposés au cours des années pour décrire l'ablation laser, la pertinence réelle de ceux-ci n'a jamais été directement établie. Pour de faibles fluences (énergie incidente par unité de surface), les mécanismes possibles sont habituellement séparés en deux classes : photo-thermiques et photo-mécaniques. La première classe est composée des mécanismes qui causent l'ablation suite à une transition de phases ou au passage du système dans un régime de métastabilité ou d'instabilité thermodynamique. Dans cette catégorie, trois mécanismes sont habituellement évoqués : la vaporisation [13], l'explosion de phase [26, 31, 32, 50, 66] et la décomposition spinodale [50, 58]. La deuxième classe contient, pour sa part, les mécanismes où l'ablation survient suite à une fracture mécanique du matériau, par exemple sous l'influence d'une onde de pression tensile, comme c'est le cas pour la spallation [66].

La vaporisation consiste simplement en la désorption de monomères ou de très petits agrégats à partir de la surface de la cible. Une grande quantité d'énergie injectée en très peu de temps peut aussi induire une décomposition complète des couches supérieures de la cible. Ce mécanisme devrait naturellement se produire pour tout apport suffisamment important d'énergie.

Par contre, l'explosion de phase est un mécanisme beaucoup plus complexe et sa pertinence dans la description du processus d'ablation est beaucoup moins évidente. Lorsque la pression à l'intérieur d'un liquide diminue en deça de la pression

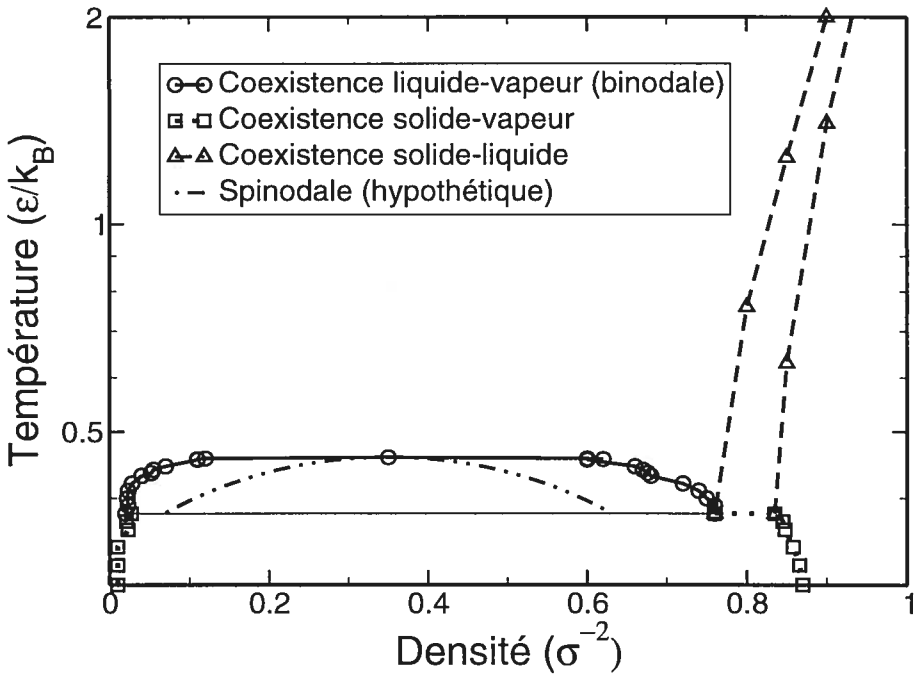

FIG. 3 – Diagramme de phase du potentiel de Lennard-Jones en deux dimensions. Voir l'annexe 2 pour les détails.

de vapeur à la saturation, l'énergie libre de la phase gaseuse devient plus faible que celle de la phase liquide. Dans un tel cas, une transition de phase devrait survenir pour favoriser la phase détenant la plus faible énergie libre, i.e. la vapeur. Cependant, la phase liquide est toujours un minimum local d'énergie libre. Le système se trouve donc dans un état métastable car une barrière énergétique le sépare de sa véritable configuration d'équilibre. Dans le diagrame de phase, de tels états sont situés entre les lignes binodales et spinodales, dans une région appellée *zone métastable* (voir la figure 3). Si la barrière énergétique séparant les deux phases est suffisamment basse, des fluctuations thermiques peuvent permettre au système de la franchir. Une bulle gaseuse se forme alors à l'intérieur du liquide par un processus appellé *germination homogène*. Or, la hauteur de la barrière énergétique est dépendante du niveau de métastabilité : elle décroit progressivement à mesure que le système se déplace de la ligne binodale vers la ligne spinodale, pour finalement disparaître quand celle-ci est atteinte. Comme le taux de germination dépend exponentiellement de la hauteur de cette barrière, de très forts taux de germination peuvent être induits par des incursions profondes en zone métastable. Dans un tel

cas, on parle *d'ébullition homogène* ("homogeneous boiling"). Ce mécanisme peut aussi causer la décomposition rapide du liquide en un ensemble de goutelettes et de gaz causant ainsi une *explosion de phase*. Si un tel mécanisme survient à la surface d'un échantillon à la suite d'un chauffage laser, il peut présumément causer l'ablation.

Finalement, la décomposition spinodale a aussi été proposée comme cause possible de l'ablation par impulsions ultra-courtes. La décomposition spinodale est en quelque sorte un cas limite de germination homogène : si le système est poussé jusqu'en zone instable (à l'intérieur de la courbe spinodale) la barrière énergétique pour la germination de bulles disparaît. La décomposition ne requiert donc plus d'activation et survient spontanément. De plus, dans cet état, la compressibilité du système devient négative, rendant celui-ci instable face à la moindre fluctuation de densité. Une décomposition rapide en goutelettes et en gaz devrait aussi survenir dans ces conditions et induire l'ablation.

D'autre part, l'ablation pourrait aussi être d'origine photo-mécaniques si des contraintes mécaniques suffisament intenses sont appliquées sur le matériau de telle sorte que sa résistance interne soit dépassée. Le mécanisme le plus souvent invoqué dans cette catégorie est la spallation [24, 66]. La spallation consiste en l'éjection de matière suite à la création de fractures à l'intérieur de l'échantillon, fractures elles-mêmes causées par le passage d'une onde de pression tensile. Dans le contexte de l'ablation laser, l'onde tensile serait crée par la réflexion sur la surface libre d'une onde compressive produite par la relaxation de l'important gradient de pression créé par le chauffage laser.

Notons aussi qu'une kyrielle d'autre mécanismes, ne faisant partie d'aucune des deux classes répertoriées ci-haut, a aussi été proposée (explosion de Coulomb dans les diélectriques par exemple [51]). Mais, encore une fois, leur pertinence n'a pas été clairement démontrée par le biais de résultats expérimentaux.

0.4 Motivation

Le débat sur l'importance de ces différents mécanisme fait toujours rage au sein de la communauté scientifique. Cette contreverse est en partie causée par la

difficulté de déterminer expérimentalement l'évolution temporelle de l'état thermodynamique du système, ce qui permettrait l'identification directe des mécanismes photo-thermiques. Bien que l'évolution de la distribution de pression au sein de l'échantillon commence à être accessible à l'aide des mesures de diffaction de rayons X résolues en temps, les profondeurs sondées sont limitées et l'interprétation des résultats difficile si cette distribution de pression est fortement inhomogène. Les mécanismes photo-mécaniques souffrent donc aussi d'un manque de confirmation directe. De plus, la distribution en taille des amas éjectés, quantité qui pourrait démontrer clairement l'existence de certains mécanismes, n'est pas mesurable pour le moment (excepté pour les très petits amas et les ions isolés). Néanmoins, les résultats de très belles expériences menées par Sokolowski-Tinten et al. [50] semblent suggérer que l'explosion de phase soit responsable de l'ablation à basse fluence. En effet, la formation de patrons d'interférence optique (anneaux de Newton) observés lors d'expériences d'ablation laser est explicable à l'aide d'un modèle d'expansion du matériau à travers la région métastable. Cependant, de l'aveu même de Sokolowski-Tinten [48], ceci ne constitue pas une preuve solide que l'ablation soit effectivement causée par l'explosion de phase dans ce régime. L'identification des mécanismes d'ablation par impulsions ultra-courtes est donc toujours sujet à polémique.

C'est dans ce contexte que nos travaux sur le sujet ont débuté. Nous avons choisi de tenter de déterminer si un modèle simple et générique pourrait nous permettre de remédier à cette situation et *d'identifier clairement les mécanismes pouvant mener à l'ablation par impulsions femtoseconde* ainsi que de *déterminer les conditions dans lesquelles chaque mécanisme prédomine*. Ces questions seront étudiées à l'aide d'un modèle numérique implémenté sous forme d'un programme de dynamique moléculaire, ce qui nous permettra d'avoir accès à des données microscopiques inaccessibles par l'expérience et de déterminer l'état thermodynamique de notre système en tout temps. La nature bidimensionnelle du système a l'avantage de permettre l'utilisation d'échantillons de grande taille, limitant ainsi l'importance des effets de taille finie. De plus, le diagramme de phase du potentiel interatomique bidimensionnel utilisé lors de cette étude est qualitativement équivalent à celui de sa contrepartie tridimensionnelle. Puisque notre étude se fonde principalement sur

l'analyse de l'évolution thermodynamique du système, nos conclusions seront donc aussi valables en trois dimensions. Bien sûr, les détails de la cinétique (lors de changements de phase par exemple) dépendent de la dimensionalité. Cependant, puisque nous nous intéressons seulement à l'identification des mécanismes généraux menant à l'ablation, ces différences sont sans conséquence. Bien que cette approche ne prenne pas en considération toute la complexité des mécanismes d'interaction laser-matière, nous croyons que les mécanismes mésoscopiques généraux propres à l'ablation d'une vaste gamme de solides peuvent être reproduits par un modèle comme celui-ci.

Le corps du mémoire sera composé de deux articles décrivant le modèle ainsi que les résultats obtenus des simulations. Le premier article, *Ablation of solids under femtosecond laser pulses* accepté pour publication dans la revue Physical Review Letters [39], présente notre modèle numérique et expose les premiers résultats de notre analyse : l'identification de 3 mécanismes d'ablation, soit l'explosion de phase, la fragmentation et la vaporisation. Cette analyse est reprise et augmentée dans le deuxième article, *Molecular-dynamics study of ablation of solids under femtosecond laser pulses* (soumis pour publication à la revue Physical Review B). La méthode de calcul de propriétés thermodynamiques locale développée lors de la présente étude y est présentée en détails. Une analyse de la dynamique d'expansion de la cible y est aussi proposée. Cette analyse montre que la vitesse d'expansion du matériau dépend de la forme de l'isentrope le long de laquelle l'expansion se produit. De plus, cet article explique la variation en fluence de la forme (de bipolaire à basse fluence à unipolaire à haute fluence) des ondes acoustiques produites par la relaxation de l'importante distribution de pression induite par le chauffage rapide de la cible à l'aide de la variation en température des propriétés élastiques de la cible. Au chapitre de l'identification des mécanismes d'ablation, cet article identifie un quatrième mécanisme, la spallation, et complète la discussion concernant les mécanismes identifiés dans le cadre du premier article. Finalement, les annexes I et II présentent, respectivement, la méthode de dynamique moléculaire ainsi que des calculs Monte Carlo réalisés pour compléter le diagramme de phase du potentiel utilisé.

CHAPITRE 1

ARTICLE *ABLATION OF SOLIDS UNDER FEMTOSECOND LASER PULSES*

Le premier chapitre de ce mémoire est constitué de l'article *Ablation of solids under femtosecond laser pulses* publié dans la revue *Physical Review Letters* [Phys. Rev. Lett., **89**, 255504 (2002)] ainsi que dans l'édition de décembre 2002 (volume 1, numéro 7) du journal électronique *Virtual Journal of Ultrafast Science*. Je suis le premier auteur de cet article, et en cette qualité j'ai : mis au point les programmes de simulation et de traitement de données, procédé à l'analyse des simulations et rédigé seul une première version de l'article. J'ai ensuite participé activement au processus d'amélioration et de raffinement en collaboration avec le coauteur de l'article, mon directeur de recherche Laurent J. Lewis.

Ablation of solids under femtosecond laser pulses

Danny Perez and Laurent J. Lewis

Département de physique et Groupe de recherche en physique et technologie de couches minces (GCM), Université de Montréal, C. P. 6128 Succursale Centre-Ville, Montréal (Québec) H3C 3J7, Canada

We study the basic mechanisms leading to ablation by femtosecond laser pulses using molecular dynamics and a simple two-dimensional Lennard-Jones model. We demonstrate that the ablation process involves three different mechanisms as a function of deposited energy. In particular, it can result from mechanical fragmentation, which does not require the system to cross any metastability or instability line. The relevance of homogeneous nucleation and vaporization for the description of ablation in this regime is also established.

The advent of femtosecond lasers in the last 15 years has enabled new insights into the realm of ultrafast dynamics [43, 12]. On the femtosecond timescale, energy can be deposited into a material faster than needed for the system to react, leading to confinement of important quantities of energy. This pushes the matter into a state of extreme non-equilibrium (near the critical point for example) and can lead to material ejection from the target, i.e., ablation.

In spite of numerous efforts [27, 50, 58, 13, 66, 20], the fundamental mechanisms that give rise to ultrashort laser ablation have still not been clearly identified. Many different possibilities have been proposed; in particular, homogeneous nucleation of gas bubbles (also known as phase explosion) has frequently been discussed [27, 50, 66]. This model predicts that the irradiated matter enters the metastable region of the phase diagram (below the binodal line), thereby causing homogeneous nucleation of gas bubbles and eventually dissociation into liquid and gas at high enough nucleation rates. Spinodal decomposition — where the system is brought into the mechanically unstable zone of the phase diagram (below the spinodal line) — has also been invoked [50, 58]; in this scenario, ablation results from the phase separation induced by density fluctuations. Finally, complete vaporization of the ejected material has been proposed [13].

These various interpretations suggest that ablation is driven by many different processes. However, experiments also show [50] that different materials behave roughly the same when irradiated by femtosecond pulses at fluences (energy deposited in the target per unit area) below the threshold for plasma formation. This would imply that some very general mechanisms are responsible for the ejection of matter. In this Letter, we study the reaction of a solid to femtosecond laser pulses and the processes that cause ablation using molecular dynamics (MD) and a simple two-dimensional Lennard-Jones model. We show that ablation involves three different processes. One of these is photo-mechanical fragmentation, identified here for the first time in the context of short-pulses laser ablation : the target disintegrates into clusters as a result of the mechanical stress imposed by the very rapid thermal expansion of the surface. The other two processes are unambiguously identified as homogeneous nucleation and vaporization. Our study provides the first clear evidence of the relevance of these processes in short-pulse laser ablation conditions.

We chose to study a two-dimensional model as this permits large systems to be explored, thereby minimizing finite-size effects ; further, there is no reason to believe that the generic features of laser ablation are different in two and three dimensions. Our system consists of 400 atomic layers in the direction perpendicular to the irradiated surface (y) and 500 layers in the lateral direction (x), for a total of 200 000 atoms initially forming a triangular lattice. The atoms interact via a Lennard-Jones (LJ) potential with ϵ and σ the usual energy and length scales, respectively. In the following, all results are in reduced units, i.e., ϵ/k_B for temperature and $\tau = (m\sigma^2/\epsilon)^{1/2}$ for time (m is the atomic mass). The LJ potential was truncated at 2.5σ. Before irradiation, the system was fully equilibrated at a low temperature, in the solid phase.

The laser pulse is incident in the y direction and taken to be spatially constant and Gaussian in time with a width at half maximum of 0.5τ ($\sim$ 100 fs). The pulse is modeled by a succession of planes, each containing a number of photons determined from the instantaneous irradiance. The energy density deposited by the laser at a given depth follows a Beer-Lambert profile $e^{-\alpha y}$ with absorption coefficient $\alpha = 0.01\sigma^{-1}$ [$\sim (20\,\mathrm{nm})^{-1}$]. During absorption, the photon energy is

transferred to "carriers". Here, a carrier is a particle that follows a Drude dynamics with a characteristic scattering time of 0.005τ ; this is too short for any significant deformation of the energy profile to take place because of carrier diffusion. When a collision between a carrier and an atom takes place, a "phonon" of energy 0.07ϵ ($\sim$ 50 meV) is transferred to the atom if the carrier possesses sufficient energy. This is accomplished by adding an appropriate component (in a random direction) to the velocity of the atom. The carrier cannot absorb energy from the environment. The photon's energy only influences the simulation through the total relaxation time of the carriers. This energy is taken to be 4.5ϵ, leading to complete relaxation of the gas of carriers within 0.3τ of the end of the pulse. The large pressure waves resulting from the rapid heating of the target are absorbed using the boundary conditions described in Ref. [65]. Periodic boundary conditions are used in the x direction. This model is not meant to reproduce light-matter interactions in a detailled manner; however it is expected to possess the features which are relevant to a "generic" description of laser ablation at fluences under the threshold for plasma formation.

We first show that ablation proceeds by different mechanisms as a function of the energy density (which varies with depth) imparted to the system and that, in a typical situation, no single process can account for ablation. To demonstrate this, the thermodynamical evolution of the system is followed in time; in this way, it is possible to locate the position (in the phase diagram) at which the creation of defects that eventually leads to ablation is initiated. In the case of strictly thermal mechanisms, this is sufficent to identify the process responsible for ablation.

In order to obtain the required information, a novel method is introduced, whereby three different thermodynamical trajectories are followed in the $\rho - T$ phase diagram. The first gives a *macroscopic* (average) view of the system, independent of the presence of clusters or pores. The other two are phase specific : a *dense branch* for atoms belonging to clusters, and a *gas branch* for isolated atoms. Clustered atoms are identified using the Hoshen-Kopelman algorithm [22], tuned so that $\rho_{\text{dense}} > \rho_c$, where ρ_c is the density at the critical point. The volume occupied by the different phases is found using the method of Ref. [52]. As we will see, the values of the densities along the different branches give the structural information (porosity

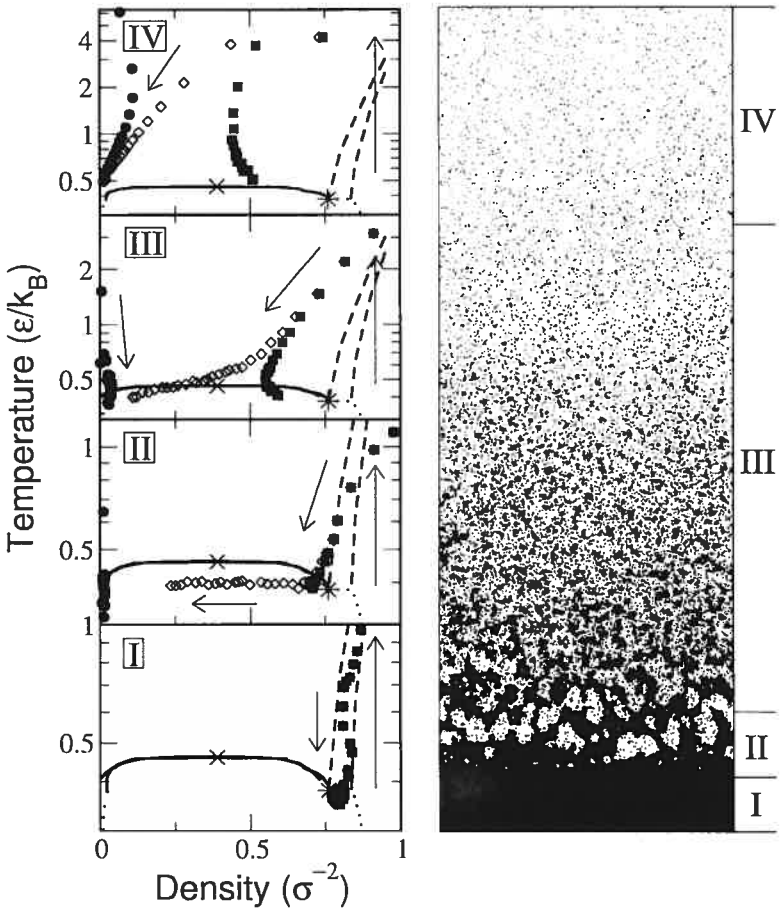

FIG. 1.1 – Left : Time evolution of the system in the $\rho - T$ plane for different effective energy densities : I) $E_{\text{eff}} = 0.7\epsilon/\sigma^2$, II) $E_{\text{eff}} = 1.2\epsilon/\sigma^2$, III) $E_{\text{eff}} = 3.0\epsilon/\sigma^2$, IV) $E_{\text{eff}} = 6.0\epsilon/\sigma^2$. Circles : gas branch ; squares : dense branch ; diamonds : macroscopic branch. Solid line : binodal line ([47]) ; dashed lines : solid-liquid coexistence lines ; dotted lines : solid-vapor coexistence lines. The critical point is marked by a cross and the triple point by a star. Arrows indicate the flow of time. Right : Snapshot of a simulation for a fluence of $F = 900\,\epsilon/\sigma$ at $t = 250\tau$ showing the topology of the system for the four different situations.

and gas content) needed to identify the onset of ablation.

Because the exponential absorption curve gives rise to a non-uniform temperature profile, thermodynamic paths were calculated as a function of depth for groups of atoms having absorbed approximately the same quantity of energy, here four-atomic-layer-thick "slices". The slices are characterized by an *effective energy density* (E_{eff}), defined as the energy per unit area remaining in the slice after relaxation of the strong thermoelastic pressure built-up by the emission of shock waves. Note that the temperatures of the slices were calculated using the velocities relative to the centers of mass. Figure 1.1 shows the thermodynamic evolution of slices typical of different regions of the target, marked I to IV, each containing many slices, which we discuss next.

The trajectories are of four types. The first, shown in Fig. 1.1(I), is typical of low absorbed energy densities ($0 < E_{\text{eff}} < 1.0\,\epsilon/\sigma^2$). After the constant-volume heating (arrow up) typical of femtosecond laser conditions, the system relaxes within the solid region of the phase diagram. The macroscopic and dense branches coincide, indicating that no voids were created in this slice. As can be verified in the right panel of Fig. 1.1, no ablation takes place in this region despite the fact that the maximum temperature reached during the simulation is larger than the critical temperature [$T_c = 0.459\,\epsilon/k_B$ [47] (~ 4000 K)]. Relaxation by expansion and conversion of heat into mechanical energy (pressure waves) is thus very efficient in this case.

The medium-energy density situation ($1.0 < E_{\text{eff}} < 1.3\,\epsilon/\sigma^2$) is illustrated in Fig. 1.1(II). The system crosses the solid-liquid coexistence region, then melts when entering the one-phase liquid region. Relaxation continues and the binodal line is crossed. In this case, homogeneous nucleation is expected to occur [23, 64] and, indeed, many signs confirm this. First, the creation of pores (marked by the split between the macroscopic and dense branches) occurs only *after* entering the metastable region, the only region in which phase explosion is possible. Second, the gas branch appears at the same moment, indicating that the pores are filled with gas. Third, the phase separation process is evident : the dense phase stays at constant temperature and density inside the metastable region, while the proportion of ga-

seous atoms steadily increases by nucleation and growth of gas bubbles (see below). This process occurs at nearly constant temperature because : (i) the free-energy barrier for nucleation of pores is very small for any significant incursion into the metastable region (and vanishes at the spinodal)[45], (ii) only a small fraction ($\sim 2\%$) of the atoms in this slice are actually converted into gas so that the latent heat spent by the system to vaporize these atoms is very small, and (iii) the expansion speed in this region in too small to induce significant cooling. The right panel of Fig. 1.1 shows that ablation follows as a result of the growth and coalescence of the bubbles.

Our thermodynamical analysis thus *directly* confirms that homogeneous nucleation [27, 50] inside the superheated liquid is responsible for ablation in this regime, in contrast with previous MD studies [66], where the occurence of homogeneous nucleation was inferred from the properties of the ejected material. Because the efficiency of the thermal confinement is typically as strong for picosecond pulses as for femtosecond ones, phase explosion is also expected to occur with longer pulses. However, this kind of trajectory is only observed in a relatively narrow band of absorbed energies, and thus phase explosion cannot solely account for ablation at fluences far above the threshold. (At the threshold fluence, region II would extend up to the surface of the target.)

Fig. 1.1(III) shows the typical evolution of the system for energies in the range $1.3 < E_{\text{eff}} < 4.5\,\epsilon/\sigma^2$. The laser pulse is now intense enough to initially push the sample to a strongly superheated solid state. Thus, melting occurs at the very beginning of the relaxation process. The trajectory differs from that for the phase explosion regime in an important manner : the macroscopic and dense branches now split way *above* the binodal line, *implying that the system has already decomposed by the time the metastable region is reached.* Homogeneous nucleation and spinodal decomposition thus cannot account for ablation in this regime. Given the large number of clusters present in the plume (see right panel of Fig. 1.1), vaporization must also be excluded. Ablation is therefore *not* caused by a photo-thermal process [27]. We will return to this crucial point below.

For energies greater than the cohesive energy of the target ($E_{\text{coh}} = 4.15\epsilon/\sigma^2$), complete atomization of the surface layers occurs. This case is presented in Fig. 1.1(IV). Here, the dense and macroscopic branches split as soon as relaxation starts, and the gaseous and macroscopic branches merge shortly after, indicating that the system behaves essentially like a gas. As can be appreciated from the right panel of Fig. 1.1, a very small number of atoms form clusters in this regions of the plume (so the behavior of the dense branch is not meaningful). This regime thus clearly correspond to a vaporization process.

We have not observed a single case where the critical point was approached while the system was homogeneous, i.e., we find no evidence for spinodal decomposition as reported in Ref. [58].

We have shown that, depending on the energy, three different mechanisms may cause ablation in the femtosecond regime. At sufficiently high fluences, all of them are effective in different regions of the target. While two of these processes — homogeneous nucleation and vaporization — are photo-thermal, the third is not. We now proceed to show that in this third regime, ablation is "photo-mechanical" and occurs by a fragmentation process.

In the energy density range where ablation is not photo-thermal, the relaxation of the very large thermoelastic stress induced by the constant volume heating of the target causes the expansion to proceed at very high speed (an appreciable fraction of the speed of sound in the medium), itself a strongly varying function of injected energy (and hence of position inside the target). This causes spatially non-uniform strain rates ($\eta = dv_{\text{translation}}/dy$) that can reach values as large as $\eta = 0.1\tau^{-1}$ ($10^{12}s^{-1}$). Under such conditions, the elastic energy stored in the expanding liquid grows very rapidly. Further, the large expansion speed *gradient* between the different slices will inhibit the diffusion mechanism by which density inhomogeneities (induced by thermal fluctuations) are usually balanced out. These inhomogeneities will thus survive and actually grow, leading the creation of internal surfaces and enabling the relaxation of some internal stresses. If enough surface is created, the initially homogeneous fluid will turn into an ensemble of clusters, and ablation follows. This strain-induced structural reorganisation is called fragmentation. It does

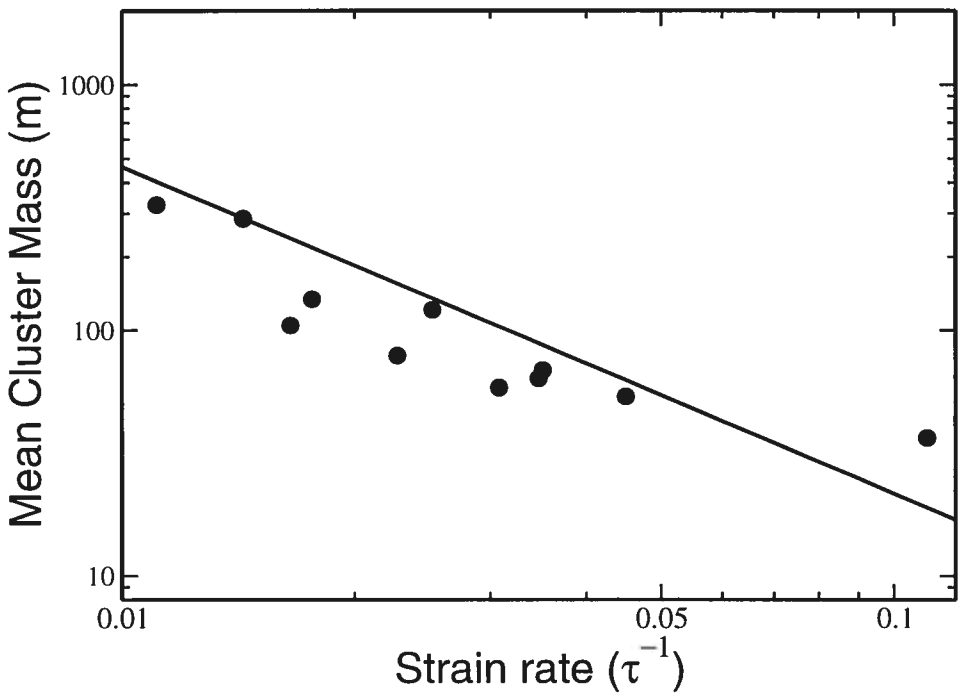

FIG. 1.2 – Mean cluster mass versus local strain rate for $F = 750\epsilon/\sigma$. The solid line is Eq. 1.1 with $\rho = 0.55\sigma^{-2}$, $\gamma = 0.4\epsilon/m$ and $\zeta = \pi/4$ (circular fragments).

not require any change of phase, nor the crossing of a metastability or instability limit, and thus can occur in supercritical conditions where phase explosion and spinodal decomposition are not possible. It differs from other photo-mechanical mechanisms (cavitation [35] or spallation [66]) because it does not involve the passage of tensile waves through the target. In fact, tensile waves do not form in our samples at high fluences.

Ashurst and Holian [3] have observed fragmentation in two and three-dimensional LJ systems under homogeneous expansion. It has also been observed in studies of the rapid heating of liquid drops [5, 54] and in experiments on the free-jet expansion of liquids [28, 4]. We now demonstrate quantitatively that fragmentation in indeed responsible for ablation in the high-energy regime.

For fragmentation, the size of the clusters formed should decrease with increasing local strain rate, as larger strain rates cause more surfaces to be created and thus smaller fragments. This is verified in Fig. 1.2 where the mean cluster mass

(at the time they formed) is plotted against the local strain rate for $F = 750\epsilon/\sigma$, and is also apparent in region III of the right panel in Fig. 1.1. In fact, there appears to be a power law dependence between the two quantities. This dependence can be quantitatively accounted for by the simple fragmentation model of Ashurst and Holian [3], which states that fragmentation results from the conversion of the internal stress stored in the expanding target into surface energy : for a uniaxial expansion in two dimensions, the mean cluster mass depends on the local strain rate as

$$M = 4\zeta\rho(r_0\gamma)^{2/3}\eta^{-4/3} \tag{1.1}$$

where ζ is a geometric factor of the order of unity, η is the strain rate, r_0 is the equilibrium bond length, and γ is the surface energy per unit mass. The same power-law dependence is predicted by the energy-minimization model of Grady [18, 3] and thus constitutes a strong signature of fragmentation. These models are also known to be correct in three dimensions, with a different scaling of the cluster mass on the strain rate.

Eq. 1.1 is plotted in Fig. 1.2, using $\rho = 0.55\sigma^{-2}$ as a typical density at fragmentation time, $\gamma = 0.4\epsilon/m$ and $\zeta = \pi/4$ (circular fragments). The model accounts precisely for the power-law dependence and the prefactor agrees with the MD data to within 30%. Given the difficulty in evaluating the different parameters entering Eq. 1.1 in such rapidly-changing conditions, the agreement is excellent. Because the fragmented state is not the equilibrium configuration at low densities and high temperatures typical of the diluted plume, many monomers are emitted from the surface of the clusters (see right panel of Fig. 1.1) in order to restore the equilibrium gaseous state. The Ashurst-Holian prediction is thus only valid at early times. Taken together with the evidence from the thermodynamical trajectories, this shows that fragmentation is indeed responsible for ablation in the non-photo-thermal regime.

As a final remark, for the thermoelastic stress to be released violently enough that important strain rates are induced in the target, the stress confinement condition ($\tau_p\alpha c < 1$ where τ_p is the pulse length and c is the speed of sound) must be respected. Since this is usually true for picosecond pulses, fragmentation should also

occur in this case. Preliminary simulations of our model system in the picosecond regime confirm this.

Our simulations therefore establish that laser ablation in the short-pulse regime involves both thermal and mechanical processes, which are effective at different deposited energies densities (and hence different depths under the surface of the target). Mechanical fragmentation is identified here for the first time in the context of short-pulse laser ablation. The relevance of homogeneous nucleation and vaporization in the description of ablation in this regime is also established.

We thank Patrick Lorazo, Ralf Meyer and Michel Meunier for numerous enlightening discussions. This work has been supported by grants from the Canadian *Natural Sciences and Engineering Research Council* (NSERC) and Québec's *Fonds québécois de la recherche sur la nature et les technologies* (NATEQ). We are indebted to the *Réseau québécois de calcul de haute performance* (RQCHP) for generous allocations of computer resources.

CHAPITRE 2

ARTICLE *MOLECULAR-DYNAMICS STUDY OF ABLATION OF SOLIDS UNDER FEMTOSECOND LASER PULSES*

Le deuxième chapitre de ce mémoire est constitué de l'article *Molecular-dynamics study of ablation of solids under femtosecond laser pulses* soumis pour publication à la revue *Physical Review B*. Je suis le premier auteur de cet article, et en cette qualité j'ai : mis au point les programmes de simulation et de traitement de données, procédé à l'analyse des simulations et rédigé seul une première version de l'article. J'ai ensuite participé activement au processus d'amélioration et de raffinement en collaboration avec le coauteur de l'article, mon directeur de recherche Laurent J. Lewis.

Molecular-dynamics study of ablation of solids under femtosecond laser pulses

Danny Perez and Laurent J. Lewis

Département de physique et Groupe de recherche en physique et technologie de couches minces (GCM), Université de Montréal, C. P. 6128 Succursale Centre-Ville, Montréal (Québec) H3C 3J7, Canada

The laser ablation process of solids under femtosecond laser pulses is studied using a two-dimensional molecular-dynamics model. The simulations show that different expansion regimes develop as a function of the injected energy. The origin of these regimes lies in changes of the thermodynamical relaxation path of the material when the intensity of the laser heating increases. The shape of the pressure waves generated as a result of the absorption of the pulse are shown to vary from bipolar at low fluence to unipolar at high fluence as a result of the decrease in tensile strength of the material at high temperatures. By combining these results with an analysis of the thermodynamical trajectories of different portions of the target, we show that four different mechanisms can account for ablation at fluences below the threshold for plasma formation, namely spallation, phase explosion, fragmentation and vaporization. These mechanisms are characterized in detail and it is demonstrated that they can occur simultaneously in different parts of the target.

2.1 Introduction

The ablation of matter from a target induced by laser pulses is a well-known technique routinely used in a number of areas. It is now appreciated that very short (femtosecond) pulses offer numerous advantages over longer pulses : the high efficiency (yield/injected energy) and the small thermal and mechanical damages inflicted to the target are invaluable characteristics for, e.g., micromachining [17, 29] and biomedical applications.[29, 24, 34] Femtosecond laser pulses are also ideal for studying the fundamental properties of matter in extreme conditions of temperature and pressure. [50, 41]

However, the basic mechanisms leading to ablation are poorly understood, largely because theoretical modeling of laser ablation is difficult. Indeed, many pro-

cesses are induced by the absorption of high quantities of energy in very short times. On a microscopic scale, these include : dielectric breakdown in transparent solids, [25] change of optical and electronic properties, [19] nonthermal melting of covalent materials, [49] and semiconductor-to-metal transitions. [9] On a mesoscopic scale, the pressure wave generation, [8, 16, 24] the thermodynamical evolution of the expanding matter, [50, 63] and the identification of the collective ejection processes [26, 31, 32, 13, 36, 50, 66, 58, 39] must all be understood in order to provide a complete picture of the phenomenon.

While a complete, microscopic description of femtosecond ablation is out of reach of present models, progress made in the study of the mechanisms leading to ablation can nevertheless have significant impacts on applications. Many mechanisms are believed to play a role in ablation below the threshold for plasma formation : photo-mechanical spallation (in organic solids), [24, 66] homogeneous nucleation of gas bubbles and phase explosion, [26, 31, 32, 50, 66, 39] spinodal decomposition, [50, 58] fragmentation,[39] and vaporization. [13]

Here we study the mesoscopic aspects of laser ablation using a simple two-dimensional molecular dynamics model. Because they determine the conditions in which ablation occurs, the expansion dynamics of the irradiated target and the generation of pressures waves will first be investigated. It will be shown that different expansion regimes appear as a function of the injected energy (and hence depth under the surface). The origin of these regimes is traced back to variations in the thermodynamical relaxation path followed by the expanding matter as the injected energy increases. It will also be shown that these regimes explain the formation (at low fluence) and disappearance (at high fluence) of the optical interference patterns observed in experiments (Newton rings). [50] Pressure waves generated during the relaxation process also suffer some changes as the fluence is increased : the profile transforms from bipolar at low fluence to unipolar at high fluence because of the loss of tensile resistance of the material (thermal softening) at high temperature. Following the preliminary results presented in Ref. [39], we show that knowledge of the precise thermodynamical evolution of the target, not easily accessible to experiment, is the key to the identification of the ablation process. Spallation, homoge-

neous nucleation, fragmentation and vaporization are shown to be relevant to the description of ablation in the femtosecond regime, and can occur simultaneously in different regions of the target. Furthermore, the occurrence of these ablation mechanisms are related to the mechanical and thermodynamical properties of the material. Finally, the dependence of the ablation depth on fluence is investigated.

The model, the method for calculating thermodynamical trajectories, and the phase diagram of the potential are first presented Section 2.2. The overall reaction of the target to the laser-induced heating is discussed in Section 2.3.1 in terms of three aspects : analysis of snapshots of the model system during the ablation process and investigation of the expansion dynamics and of the generation of pressure waves. Identification and discussion of the different ablation processes is presented in Section 2.3.2. Finally, the variation of the ablation depth with fluence is examined in Section 2.3.3 before concluding.

2.2 Computational methods

2.2.1 Model

We study the ablation process using molecular-dynamics simulations [1] in two dimensions, thereby enabling large systems to be considered, thus minimizing finite-size effects, which could be a problem in the case of homogeneous nucleation, as the system has to be able to accommodate many critical nuclei. Furthermore, there is no reason to expect the mechanisms of ablation to depend in a significant manner on dimensionality. Simulations were carried out using samples with either 400 or 800 atomic layers in the y direction (parallel to the incident laser pulse) and 500 layers in the x direction, for a total of 200 000 or 400 000 atoms initially forming a triangular lattice. The lattice was thermalized in the low temperature solid state before beginning the simulations. The atoms interact via a simple Lennard-Jones potential adjusted so as to vanish at the cutoff distance r_c :

$$\begin{aligned} \phi_{\mathrm{LJ}}(r) = \; & 4\epsilon[(\sigma/r)^{12} - (\sigma/r)^6 \qquad r \leq r_c \\ & -(\sigma/r_c)^{12} + (\sigma/r_c)^6] \\ \phi_{\mathrm{LJ}}(r) = \; & 0 \qquad\qquad\qquad\qquad\quad r > r_c \end{aligned}$$

with ϵ and σ the usual energy and length scales, respectively. We used $r_c = 2.5\sigma$. In the following, all results are reported in reduced units, i.e., ϵ/k_B for temperature and $\tau = (m\sigma^2/\epsilon)^{1/2}$ for time (m is the atomic mass). This potential was chosen for its simplicity and because it captures the essential features of realistic interatomic potentials.

The laser pulse, incident on the target from the y direction, is uniform in space and has a Gaussian temporal profile with a width at half maximum of $\Delta t = 0.5\tau$ ($\sim$ 100 fs). The pulse is modeled as an ensemble of discrete photons of energy 4.5ϵ, emitted using appropriate distributions. The energy absorption inside the target follows a Beer-Lambert law ($I = I_0 e^{-\alpha y}$) where α is the absorption coefficient; two values were examined : $\alpha = 0.01$ or $0.002\sigma^{-1}$ ($\simeq 20$ or $\simeq 100\,\mathrm{nm}^{-1}$). Absorption of the photons by the target proceeds by the transfer of its energy to a "carrier". Here, a carrier is a particle which follows a Drude dynamics, i.e., the dynamics is governed by successive collisions determined by a characteristic scattering time taken to be 0.005τ. At each collision, a "phonon" of energy 0.07ϵ ($\sim$ 50 meV) is transferred from the carrier to the nearest atom if the carrier possesses sufficient energy. This is accomplished by adding an appropriate component to the velocity of the atom in a random direction. The carriers cannot absorb energy from the target. It must be stressed that it is not our goal to mimic realistic carrier dynamics, but only to model in a physically relevant manner the rate at which the energy is deposited.

The rapid heating of the target following the absorption of light generates important pressure waves that must be dealt with in a proper way to avoid artifacts in the simulations. In order to do this, we use the absorbing boundary conditions proposed in Ref. [65] in the y direction; periodic boundary conditions are used in the x direction. A Langevin heat bath is also used at the bottom of the target in order to mimic heat diffusion outside of the simulation cell.

As stated earlier, this simple model is not meant to reproduce light-matter interactions in a rigorous way. However, we expect the generic mesoscopic features of the ablation process to be well described by the model for fluences below the threshold for plasma formation.

2.2.2 Calculation of local thermodynamical properties

The analysis which follows relies heavily on local, phase-specific thermodynamical properties of small sections of the system. In particular, we are interested in groups of atoms that have absorbed similar quantities of energy so as to determine their common thermodynamical evolution. Care is needed in computing this; the method used to do so is described here.

The target is separated into "slices" perpendicular to the incident light; we chose them to be four-layer thick. This grouping is preserved during the whole simulation; however, only the N atoms lying within one standard deviation of the mean y position of the atoms in the slice are taken as representative and used to compute the local thermodynamical quantities ρ, P and T as a function of time. The temperature and pressure are obtained using the standard formulas :

$$T = \frac{m}{2N} \sum_{i=1}^{N} (v_i - v_{cm})^2 \tag{2.1}$$

and

$$P = A^{-1}(\mathcal{W} + NT), \tag{2.2}$$

where v_{cm} is the center-of-mass velocity of the slice, A the area occupied by the slice, and $\mathcal{W}$ the virial sum. The area occupied by such small sub-systems is most difficult to obtain (and even to define). To circumvent this difficulty, a tessellation of space into Voronoi polygons centered around atomic positions is used, as shown in Fig. 2.1.

The area occupied by a group of atoms is defined as the sum of the areas of their respective polygons. This procedure is free from arbitrary parameters. The trajectories obtained in this way will be referred to as *average*, as they give a *macroscopic view* of the system, independent of the presence of pores or clusters.

Inhomogeneities can (and will) develop during the ablation process; therefore it is desirable to follow the evolution of the clusters and of the gas separately using a *condensed* and a *gas* branch. In order to do this, clustered and isolated atoms are first identified using the Hoshen-Kopelman algorithm [22]. The clustering

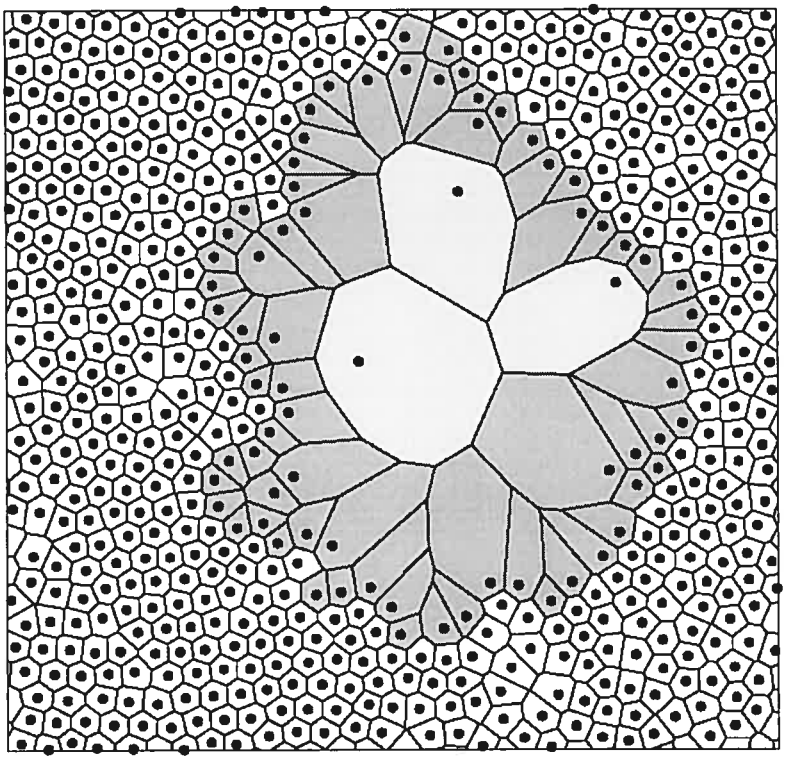

FIG. 2.1 – Phase-specific density calculation. White : condensed bulk atoms; dark gray : condensed surface atoms; light gray : isolated atoms.

radius is chosen so that the triple point density separates the gas and condensed regions. The condensed (clustered) atoms are then separated into two categories : bulk (fully coordinated) and surface (under-coordinated) (see Fig. 2.1). The area occupied by the condense phase is defined as the total number of clustered atoms times the mean area of the Voronoi polygons for atoms in the bulk subgroup. The difference between the total area of the slice and the area occupied by the condense phase is attributed to the gas phase. With this procedure, it is possible to obtain phase-specific thermodynamical quantities using Eqs. 2.1 and 2.2 by averaging over the appropriate subgroup of atoms. For the temperature on the condensed branch, different v_{cm} are used for each cluster.

As will be shown in Section 2.3.2, the use of these three different thermodynamical trajectories (average, condensed and gas) allows the type of process responsible for the ablation of a particular slice to be identified, because a correlation between the formation of voids inside the target (which causes the average and condense

branches to split) and the instantaneous thermodynamical state of the system can be established.

2.2.3 Phase diagram of the two-dimensional truncated and shifted LJ system

In order for the thermodynamical trajectory calculations to be useful, the phase diagram of our model system must be known. Because the phase diagram is very sensitive to small modifications of the potential (like truncation and shifting), the abundant data published for the full LJ potential cannot be employed here and calculations had to be performed in order to complete the data available for the particular version of the LJ potential we use. The phase diagram we obtained is presented in Fig. 2.2. The binodal (liquid-vapor coexistence) line was partially taken from Ref. [47] and completed down to the triple point using Gibbs ensemble Monte Carlo simulations.[37] The solid-vapor coexistence region was also obtained using this method. Because the Gibbs ensemble Monte Carlo method does not work well at high density, the position of the solid-liquid coexistence region was inferred from the temperature change of the entropy, which was computed with the method of Ref. [47]. The isentropes obtained in this way were also used to obtain the speed of sound inside the LJ system as a function of temperature and density $[c^2 = (\partial P/\partial \rho)_S]$.

2.3 Results

2.3.1 Reaction of the target after the absorption of a pulse

We first discuss the global reaction of the system after the absorption of the pulse. This analysis develops along three lines. First, using snapshots from the simulations, we show that different morphological and dynamical features are observed in the target depending on the energy density locally absorbed. Second, the expansion dynamics is discussed and the origin of the different regimes is linked to changes in the thermodynamical relaxation paths of the material. We also confirm the model proposed by Sokolowski-Tinten et al.[50] to explain the formation

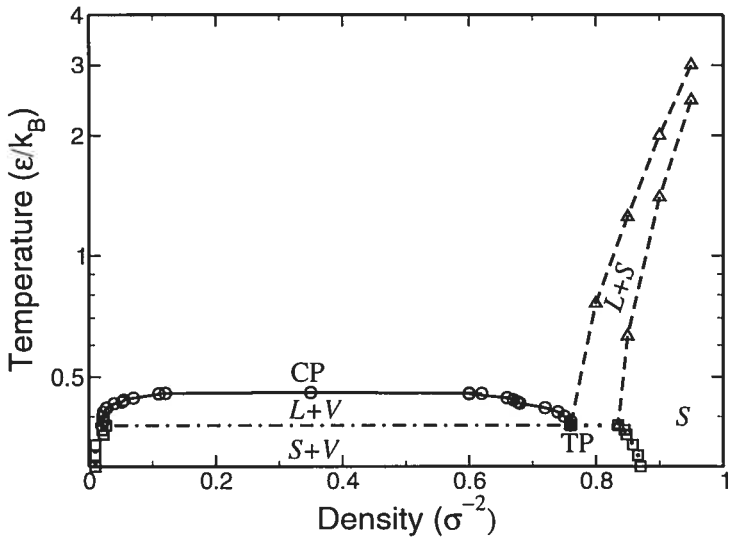

FIG. 2.2 – Phase diagram of the 2D truncated and shifted Lennard-Jones potential in the $\rho - T$ plane. Full line and circles : binodal line (liquid-vapor coexistence); dotted line and squares : solid-vapor coexistence line; dashed line and triangles : solid-liquid coexistence line; dash-dotted line : boundary of the solid-vapor and liquid-vapor coexistence regions. The italic letters refer the the phases in each regions (S, L, V : solid, liquid and vapor respectively). **CP** : critical point, **TP** : triple point.

of optical interference patterns during ablation. Third, and last, variations of the characteristics of the acoustic waves generated by the relaxation of the thermoelastic pressure distribution induced by the laser heating are analysed and related to the mechanical properties of the material.

2.3.1.1 Visual analysis

Figures 2.3 and 2.4 show snapshots the of simulations for the system with 400 000 atoms and a small absorption coefficient ($\alpha = 0.002\,\sigma^{-1}$) at different moments during the simulation. The evolution of the system at low fluence ($F = 1.2\,F_{\rm th}$, where $F_{\rm th}$ is the threshold fluence for ablation) is discussed first in Fig. 2.3. The laser pulse is fired during the first 2τ. In spite of the drastic heating which occurs during the relaxation of the carrier gas, the target does not react before about $t = 5\tau$. At this moment, the important pressure build-up generated by the isochoric heating is relaxed by the emission of a pressure wave (see later) and the expansion

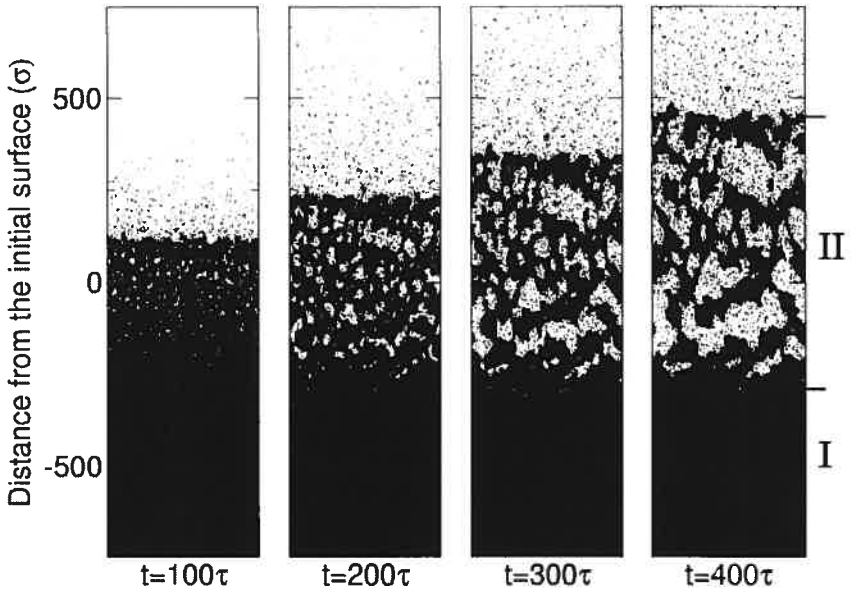

FIG. 2.3 – Snapshots of a simulation with $F = 900\epsilon/\sigma = 1.2\,F_{\rm th}$ and $\alpha = 0.002\sigma^{-1}$. Roman numerals identify different regions of the target (see text).

of the target starts. Emission of monomers from the surface has also begun by then. At around $t = 100\tau$ (first snapshot), nucleation of small pores is initiated in the surface region. At $t = 200\tau$, it is apparent that these voids are filled with gas. During the next 200τ, intense growth and coalescence occur so that the size of the voids increases rapidly. This finally leads to the ablation of large liquid droplets from the topmost 300σ of the target. An interesting feature of the plume in this case is that the matter-vacuum interface progresses slowly and stays relatively sharp for a long period of time. We will show later that this can explain the observation of optical interference patterns in short-pulse laser ablation experiments. [50] Despite the exponential temperature profile initially imposed by the laser pulse, the reaction of the system is remarkably homogeneous : the size of pores and their gas content do not seem to depend strongly on the depth below the surface. In this case only two regions are distinguishable : the non-ablated solid region and the porous region, numbered I and II respectively.

Figure 2.4 shows that the situation is somewhat more complex at higher fluence

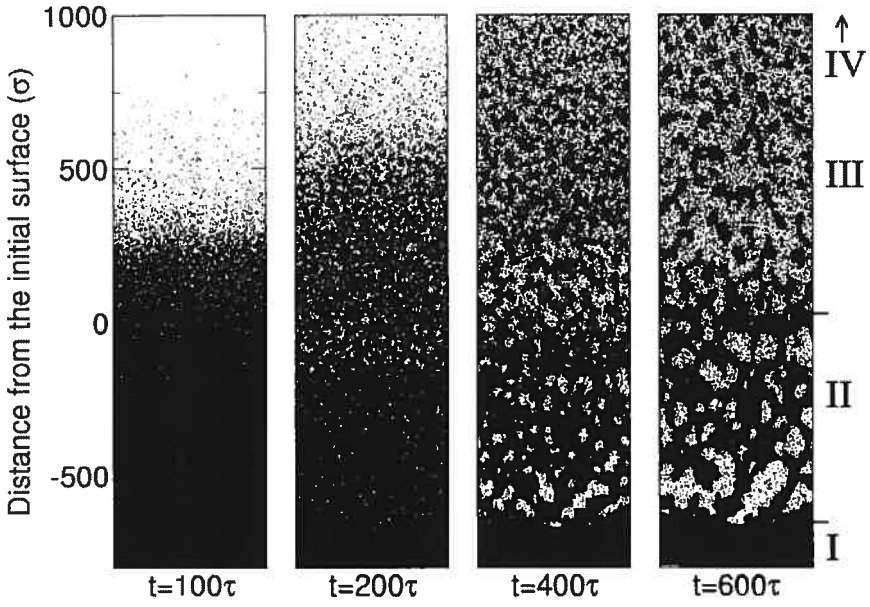

FIG. 2.4 – Snapshots of a simulation with $F = 2100\epsilon/\sigma = 2.8\,F_{\rm th}$ and $\alpha = 0.002\sigma^{-1}$. Roman numerals identify different regions of the target. Region IV is the gaseous region (out of the range of the last snapshot).

($F = 2.8\,F_{\rm th}$). We see from the first snapshot ($t = 100\tau$) that expansion and emission of monomers from the surface is now much more intense than in the previous case. Again, small voids are present near the surface at this moment. However, by $t = 200\tau$, the coalescence of these voids causes the fast-expanding surface region to decompose into an ensemble of small clusters. Evaporation from the surface of the clusters quickly fills the surrounding area with gas. By then, the front matter-vacuum interface is already destroyed, i.e., the density now varies continuously with position. At $t = 400\tau$, many gas-filled pores develop in the bottom section of the target; the morphology of this section is very much like the surface region of Fig. 2.3. Finally, at $t = 600\tau$, the pores coalesce and induce the ejection of this part of the target. At this moment, the cluster creation process in the top part of the target is completed. Now four region are present : the non-ablated solid region I, the porous region II, the cluster-filled region III and a purely gaseous region IV (out of the range of the last snapshot). By comparing the snapshots, we see that

each region expands at a different velocity : as it does at low fluence, region II expands slowly compared to regions III and IV. The strongly-varying morphologies and expansion speeds of the different regions suggest that the ablation mechanisms might be specific to the energy density absorbed, so that many mechanisms may be effective simultaneously at different depths. It will be shown in section 2.3.2 that this is indeed the case. First, however, we study the origin of these different expansion regimes. This is required in order to understand the conditions in which ablation occurs.

2.3.1.2 Expansion dynamics

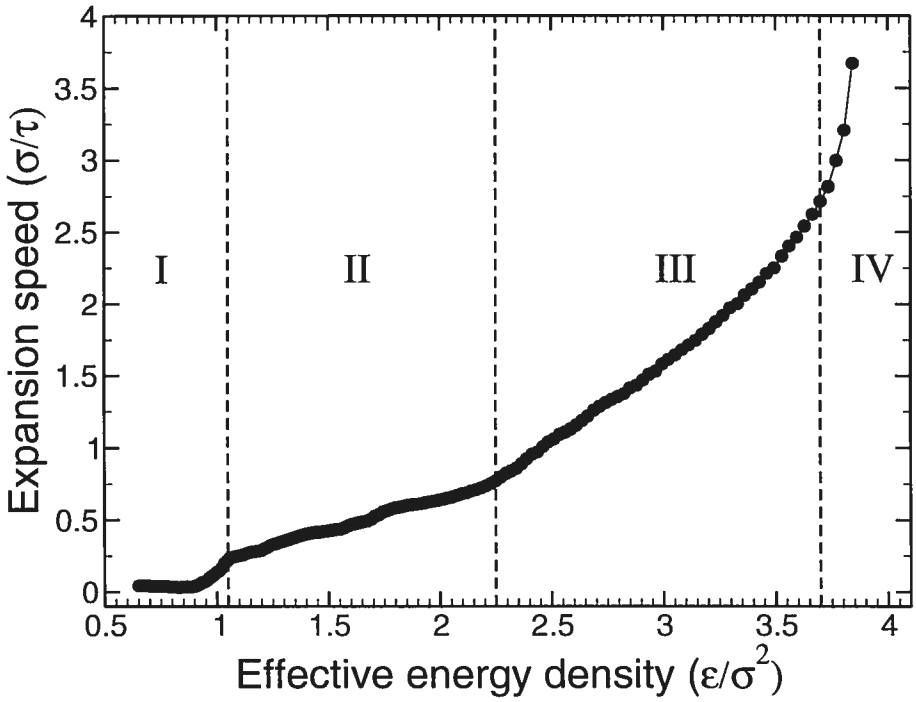

FIG. 2.5 – Expansion speed versus effective energy density for a simulation with $F = 2100\,\epsilon/\sigma = 2.8\,F_{\rm th}$ and $\alpha = 0.002\sigma^{-1}$. Roman numerals refer to the regions of the target identified in Figs. 2.3 and 2.4.

The expansion speed profile for the simulation presented in Fig. 2.4 is shown in Fig. 2.5. The data is plotted against the *effective energy density* ($E_{\rm eff}$), defined as the total energy density injected by the laser minus the energy drained during the formation of the pressure waves. $E_{\rm eff}$ thus represent the *thermal* energy stored

at different points in the target. The speeds presented in Fig. 2.5 were obtained by averaging over the quasi-steady velocity profile that establishes soon after the passage of the pressure wave. The different expansion regimes are visible in this figure. It will be shown below that each regime is associated with a specific type of thermodynamical relaxation path. In region I (unablated solid) the expansion proceeds at very low speed. A sudden increase in the expansion speed at $E_{\text{eff}} = 1.0\epsilon/\sigma^2$ marks the onset of region II, where the expansion speed depends weakly on E_{eff}. This behavior changes again around $E_{\text{eff}} = 2.25\epsilon/\sigma^2$, where region III begins. From this point on, the expansion speed increases with E_{eff} at a much larger rate. Finally, in region IV, the expansion proceeds at a very high speed, typical of the free expansion of a gas.

Because the expansion is mainly driven by the relaxation of the thermoelastic pressure formed during the heating, higher energies will naturally imply higher pressures and hence higher expansion speeds. However, since the induced thermoelastic pressure increases linearly with the injected energy, [36] the formation of distinct expansion regimes cannot be totally explained using a simple pressure relaxation argument. It will now be shown that the origin of these different regimes lies in the change of the thermodynamical relaxation paths as the injected energy increases.

Indeed, Fig. 2.6 reveals that each expansion regime is associated with a precise type of thermodynamical trajectory. The average trajectories in this figure are typical of slices found inside regions I to IV. In region I, the relaxation (following the constant volume heating of the target) proceeds totally within the solid region of the phase diagram (cf. Fig. 2.2). As this region is not ablated, the final density remains high. The onset of region II is linked to an important change in the thermodynamical trajectory : the target now melts during relaxation. The sudden increase in the expansion speed around $E_{\text{eff}} = 1.0\epsilon/\sigma^2$ is thus caused by the abrupt change of volume during the phase transition. Inspection of the samples confirms that this value of E_{eff} indeed marks the boundary between the liquid and solid regions of the target. Further, all trajectories in this region also cross the binodal line between the triple point and the critical point. After crossing the coexistence line, the relaxation continues quasi-isothermally within the liquid-vapor metastable

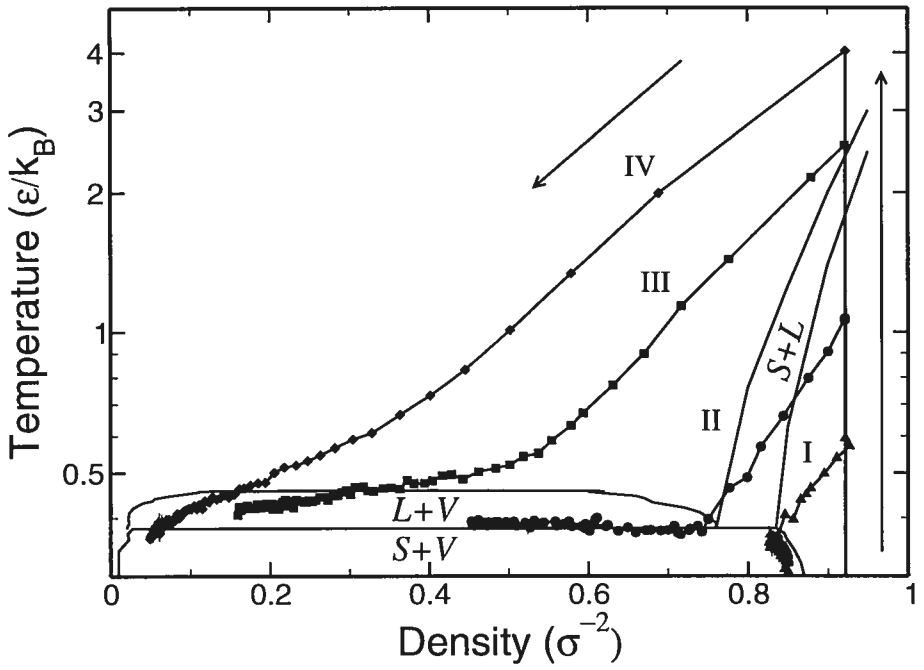

FIG. 2.6 – Examples of macroscopic thermodynamical trajectories in different regions of the target, projected in the $\rho - T$ plane. Roman numerals refer to the regions of the target identified in Figs. 2.3 and 2.4. Arrows indicate the flow of time.

region.

Another important change marks the beginning of region III : the transition from sub to super-critical relaxation. Note that, in this case, the late part of the relaxation is no longer isothermal. Finally, in region IV, the relaxation occurs along perfect-gas-like isentropes ($T \propto \rho^{2/3}$), consistent with the diluted-gas nature of the slices during expansion in this region (see Fig. 2.4).

The relation between the expansion speed and the thermodynamical relaxation path can be studied within a simplified scenario. Consider a semi-infinite homogeneously-heated layer initially at uniform density ρ_i. The adiabatic expansion of the material into the vacuum can be described by a self-similar rarefaction wave (SSRW), [30, 2] whereby the expansion along the isentrope S at density ρ_f proceeds at speed :

$$u(\rho_f, S) = \int_{\rho_i}^{\rho_f} \left(\frac{c(\rho)}{\rho}\right)_S \mathrm{d}\rho = \int_{\rho_i}^{\rho_f} \left(\frac{\partial P}{\partial \rho}\right)_S^{1/2} \frac{\mathrm{d}\rho}{\rho}, \tag{2.3}$$

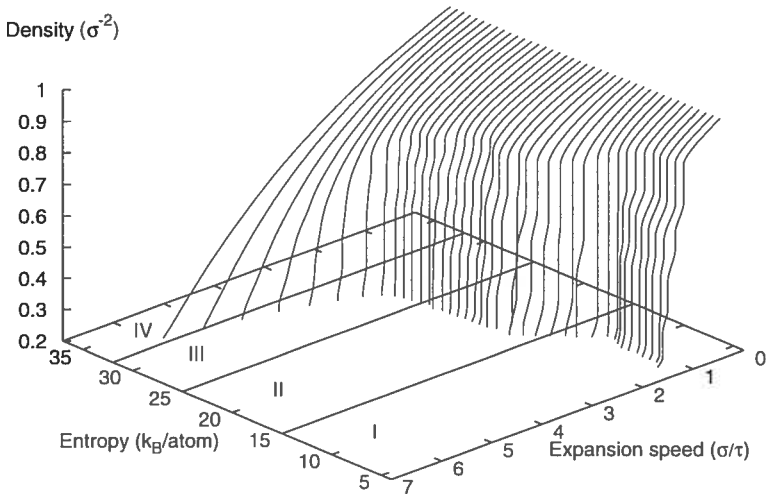

FIG. 2.7 – Density dependence of the expansion speed $u(\rho_f, S)$ as a function of entropy for a self-similar rarefaction wave with $\rho_i = 0.92\,\sigma^{-2}$. Roman numerals refer to the regions of the target identified in Figs. 2.3 and 2.4.

with $c(\rho)$ the speed of sound on the isentrope. The rarefaction (density-decrease) wave is said to be self-similar because the density profile depends solely on a similarity variable $\xi = y/t$, i.e., the dynamics are obtained by simply rescaling the $t = 0$ profile. Eq. 2.3 shows that the shape of the isentropes followed during relaxation is crucial for the dynamics of the expansion : flat isentropes (in the $\rho - P$ plane) cause the expansion to proceed slowly while important pressure variations along the isentrope cause a rapid expansion. $u(\rho_f, S)$ was computed along several isentrope (obtained with the method of Ref. [44]) and the results are shown in Fig. 2.7.

A striking feature of these results is the formation of two expansion speed plateaus at low entropy. It was shown by Anisimov et al.[2] that this phenomenon occurs because, in the solid-vapor and liquid-vapor coexistence regions, the speed of sound drops sharply, so that $u(\rho_f, S)$ is practically independent of ρ_f below a certain density (see Eq. 2.3). However, as the entropy increases to super-critical values, the abrupt decrease of the speed of sound does not occur anymore and the resulting expansion speeds can take very high values. Note that the variation of the expansion speed with entropy is also very large in the latter case.

While Eq. 2.3 is strictly valid only in the homogeneous heating limit ($\alpha \to 0$, i.e., only one $u(\rho_f, S)$ curve is followed during the expansion), the qualitative behavior it predicts gives important physical insights into the more complex expansion dynamics for finite α. In fact, there is a one-to-one correspondence between the regimes observed in the SSRW model and those identified in Fig. 2.5 First, both Figs. 2.5 and 2.7 show two low-speed, weakly entropy-dependent expansion regimes at low entropy (regions I and II) and an increase in $\mathrm{d}u/\mathrm{d}E_{\mathrm{eff}}$ as the expansion becomes super-critical (regions III and IV). Second, these regimes occur for the same entropy ranges in the SSRW model that in the finite α case. The connection between the entropy and the effective energy density is obtained through the comparison of different thermodynamical trajectories (and hence effective energy densities) with the isentropes we computed. The qualitative behavior of the expansion speed at finite α thus locally follows that predicted in the SSRW limit : variations of the expansion speed are clearly caused by significant changes in the shape of the thermodynamical relaxation paths as the effective energy (and hence entropy) increases. We will see later that the presence of these different regimes have important consequences for the ablation process.

It can be shown [2] that the density profile $[\rho(y,t)]$ for expansion along a single isentrope in the SSRW model is given by the solution of :

$$\xi = \int_{\rho_i}^{\rho} \left(\frac{c(\rho)}{\rho}\right)_S \mathrm{d}\rho - c(\rho) = u(\rho) - c(\rho). \tag{2.4}$$

Because in the present case the heating profiles are not constant but exponentially decreasing, the SSRW model cannot be used to predict the evolution of the density during the whole expansion process. However, as can be seen from Fig. 2.7, $u(\rho, S)$ [and hence $c(\rho)$] is nearly independent of S in the range $15 < S < 25\, k_B/\mathrm{atom}$ (region II). The density profile should therefore follow the SSRW prediction as long as the wave runs through regions within this entropy range.

A comparison is carried out on in Fig. 2.8 where the SSRW profile and the simulations results for the target of Fig. 2.3 are presented. The two indeed agree closely during the early stages of the expansion. The self-similar nature of the wave is destroyed at later time when the wave propagates further into the target i.e.,

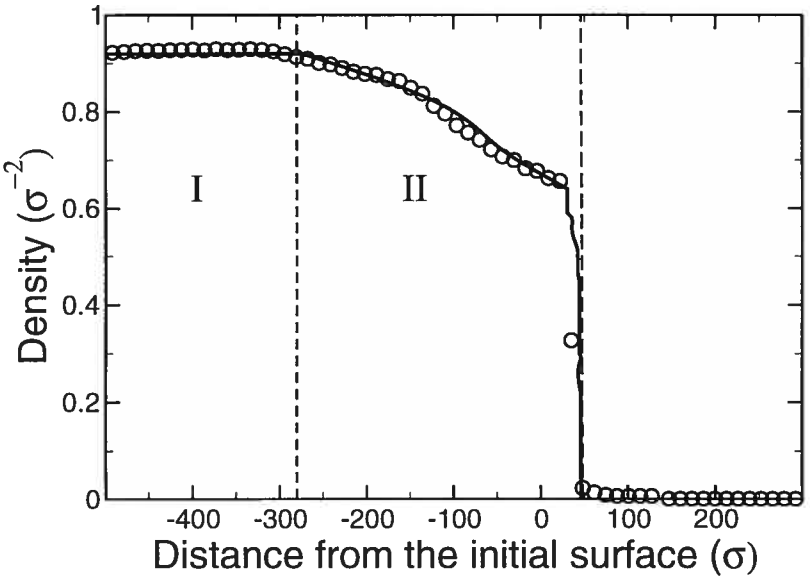

FIG. 2.8 – Density profile at $t = 40\tau$ for $F = 900\,\epsilon/\sigma$ and $\alpha = 0.002\sigma^{-1}$. Full line : self-similar rarefaction wave profile; circles : measured profile. Roman numerals refer to the regions of the target identified in Fig. 2.3 and 2.4.

into region I.

Fig. 2.8 also shows that, as demonstrated in Ref. [2], the SSRW density profile exhibits a very sharp matter-vacuum interface when expansion proceeds through the liquid-vapor coexistence region (e.g., region II). Sokolowski-Tinten et al [50] suggested that a second sharp density discontinuity would form as the rarefaction wave reaches the boundary of the solid, unablated material. If this is the case, the two discontinuities would serve as optical interfaces and hence explain the observation of interference patterns (Newton rings) under normal-incidence optical microscopy during short-pulse laser ablation experiments. [50]

Fig. 2.9(a) shows that this interpretation is correct. This figure presents the density profiles of the target of Fig. 2.3 at different times through the simulation. Here, the expansion proceeds along isentropes which cross the binodal line at the right of the critical point (Region II extends up to the surface of the target). The first profile ($t = 40\tau$) corresponds to that of Fig. 2.8. At $t = 100\tau$, the matter

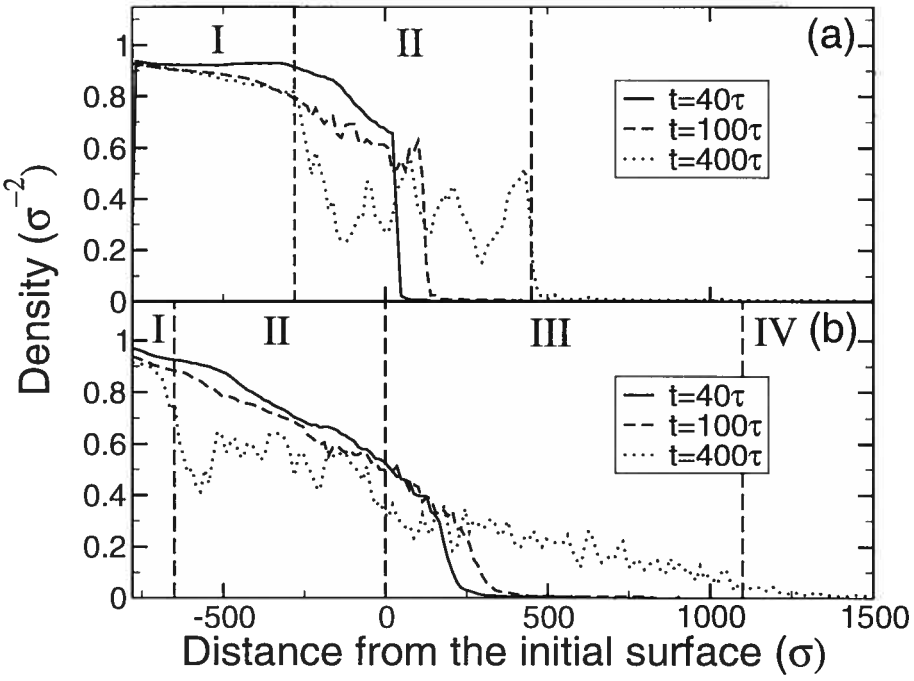

FIG. 2.9 – Density profile at different times for $\alpha = 0.002\sigma^{-1}$: (a), $F = 900\,\epsilon/\sigma$; (b), $F = 2100\,\epsilon/\sigma$. The roman numerals show the extent of the regions of the target identified in Figs. 2.3 and 2.4 at $t = 400\tau$.

at the tail of the wave — the matter-vacuum interface — enters the liquid-vapor metastable region and the nucleation of gas bubbles begins. At this same time, the rarefaction wave reaches the boundary of the nonablating region and the self-similar character of the flow is lost. At this moment, the expansion speed difference between the unablated region I and the expanding region II (see Figs. 2.5 and 2.7) causes the formation of a second density discontinuity. This discontinuity is fully formed at $t = 400\tau$. The figure also shows that the matter-vacuum interface remains sharp during the expansion, even after the self-similar character of the wave is lost. The inhomogeneous phase (region II of Fig. 2.3) trapped between the two interfaces is thought to possess the optical properties — high refraction index and low absorption coefficient — required to explain the observation of high-contrast optical interference pattern. [50] The density oscillations in region II are to a large extent caused by statistical fluctuations arising from the finite size of the sample. Our simulations therefore confirm the mechanisms proposed by Sokolowski-Tinten et al. [50] to explain the formation of Newton rings.

However, it is evident from Fig. 2.4 that the matter-vacuum interface can no longer be sustained when the fluence increases to a point where relaxation occurs along supercritical isentropes, i.e., in regions III and IV. Fig. 2.9(b) shows the changes of the density profile in this case. The evolution is now much more rapid : the rarefaction wave moves quickly and the ablation front is already blunt by $t = 40\tau$. At $t = 400\tau$ the front interface is totally lost so that the density drops continuously from the bulk value to the vacuum. The strong dependence of the expansion speed on energy in this region is responsible for the destruction of the matter-vacuum interface. This effect is predicted by the SSRW model : for a sharp front to form, the expansion speed of the material is required to depend only weakly on the density over a wide density range. [2] Since this is not the case for supercritical isentropes, the SSRW density profile shows a gradual decrease. As a result, interference patterns are not expected to form under these conditions. The disappearance of Newton rings at high fluence is indeed observed experimentally ; [11] our simulations clearly establish that the onset of supercritical expansion in the surface region of the target is responsible for this behavior.

To summarize this section, we have shown that the expansion dynamics of the plume is closely related to the thermodynamical relaxation path along which the material evolves. For relaxation through the solid or the liquid-vapor metastable region, the expansion speed is small and weakly dependent on the isentrope on which expansion proceeds. In contrast, high-speed, strongly energy-dependent expansion occurs for large injected energies. These results are in qualitative agreement with the predicted dependence of the expansion speed on the entropy in the SSRW limit, and are consistent with the formation of Newton rings at low fluence and their disappearance at high fluence, as observed experimentally.

2.3.1.3 Pressure wave generation

In the previous section, we have shown that the primary reaction of the system to the absorption of the pulse is to expand in order to relieve the important thermoelastic pressure build-up induced by the constant-volume heating of the target. However, the material also relaxes by emitting strong pressure waves. It has been

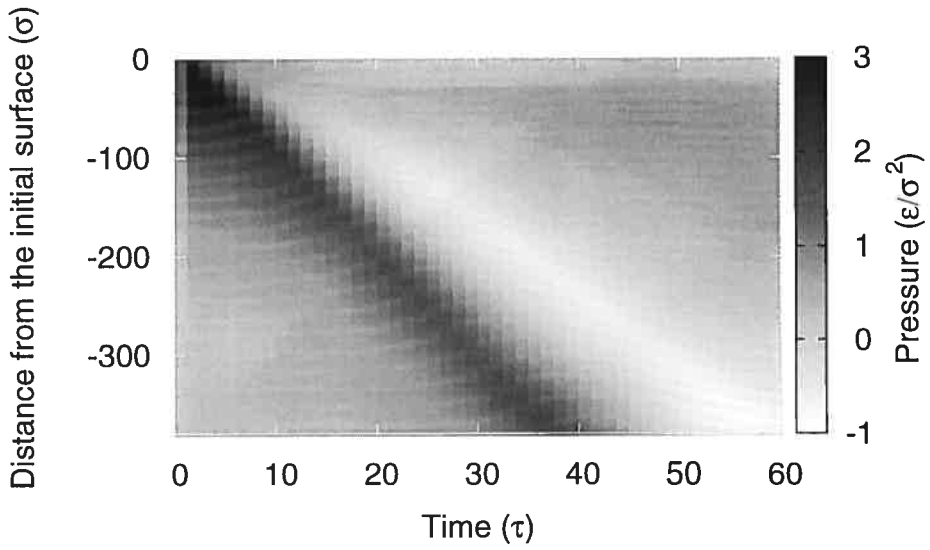

FIG. 2.10 – Pressure in the target as a function of time and position ; $F = 90\epsilon/\sigma$, $\alpha = 0.01\sigma^{-1}$.

suggested that these waves could play an important role in the ablation process ; [34, 24, 36, 66] we now discuss their properties and examine how their shape changes as the fluence increases. It will be shown that a tensile component forms at low fluences but practically disappears as fluence is increased because of the thermal softening of the material in the surface region. Thus, tensile-wave-mediated effects (like spallation) should be observed only at low fluences.

Relaxation of the thermoelastic stress occurs initially by the emission of two compressive pressure waves : one heading toward the free surface and the other toward the bulk.[8, 16, 66] The wave incident on the free surface is reflected back and becomes tensile (negative pressure). The tensile component however does not fully form before the reflected wave reaches a distance of about one penetration depth under the surface.[8] The resulting acoustic wave thus possesses a bipolar profile : a compressive maximum followed by a tensile component. [8] This is clearly visible in Fig. 2.10, which shows the evolution of the pressure inside the target for a fluence below the threshold for ablation. However, it is also apparent that the tensile component is weaker and less sharp than the compressive one. For the

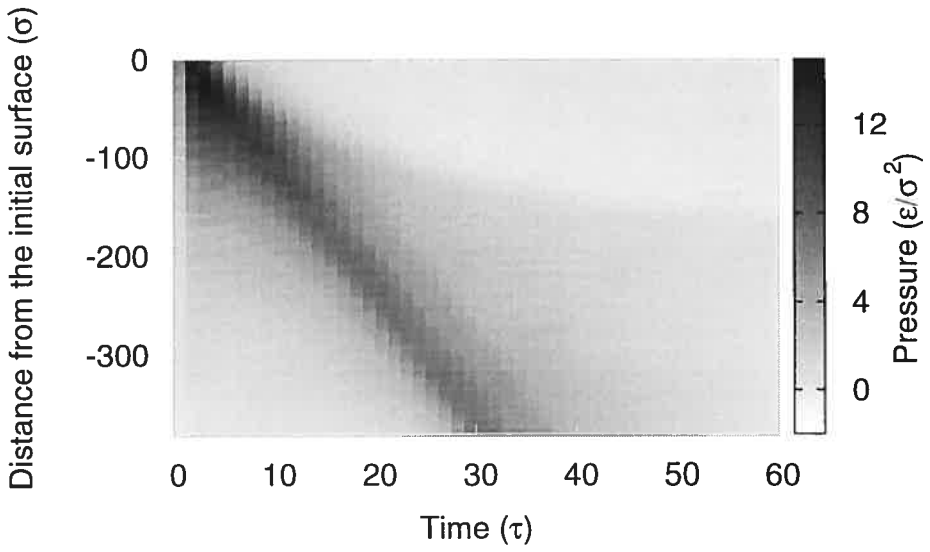

FIG. 2.11 – Pressure in the target as a function of time and position ; $F = 450\epsilon/\sigma$, $\alpha = 0.01\sigma^{-1}$.

excellent stress confinement achieved here ($\alpha c\Delta t \simeq 0.08$), a symmetric profile would be expected. This indicates that, even at modest fluences, the pressure waves are too intense to be reflected elastically from the free surface : a fraction of the energy of the incident wave is used for the creation of defects or inelastic deformations in the surface region during reflection.

Figure 2.11 shows that, at higher fluences (above the threshold for ablation), the pressure profile becomes unipolar : the tensile component disappears completely. The wave incident on the free surface is thus totally dissipated in the surface region so that no reflection occurs. The tensile stress region visible in this figure is not induced by an elastic wave, but by the progression of the melt front which initially propagates at the speed of sound, and later on slows down and finally stops around $y = -120\,\sigma$.

Figure 2.12 establishes the preceding observations on a more quantitative basis by showing the dependence on fluence of the peak maximum and minimum pressures ($P_{\max}$ and $P_{\min}$, respectively) measured inside the sample. $P_{\max}$ is found to grow linearly with fluence, as expected for a thermoelastic wave generation pro-

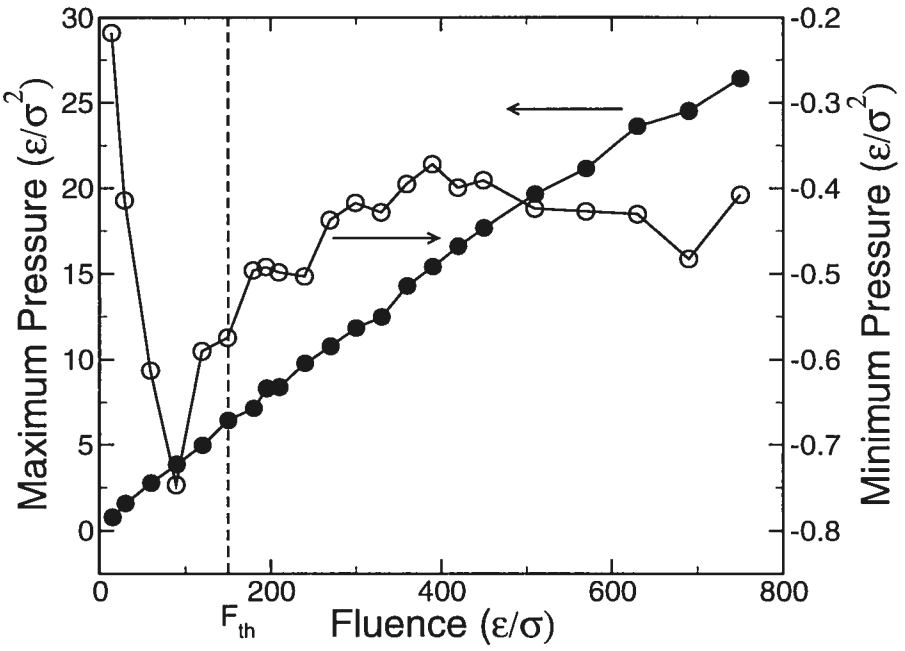

FIG. 2.12 – Maximum (filled circles) and minimum (empty circles) pressure reached inside the target, $\alpha = 0.01\sigma^{-1}$. The dashed line marks the threshold for ablation.

cess. In the case of an instantaneous heating, $P_{\max} = \alpha\Gamma F$ with Γ the Grüneisen parameter of the material. However, the behavior of $P_{\min}$ is much more complex : it initially decreases until $F = 90\epsilon/\sigma$, then grows and finally saturates around $P_{\min} = -0.45\epsilon/\sigma^2$ for $F > 200\epsilon/\sigma$. As stated earlier, if reflection on the free surface is total, $P_{\min}$ should also decrease linearly with fluence for such short pulses. The increase in $P_{\min}$ thus indicates again that the reflection of the pressure wave is not elastic above a certain threshold. Indeed, in the interval $90\epsilon/\sigma < F < 150\epsilon/\sigma$, we observe a damage-without-ablation regime — small pores nucleate near the surface, but in insufficient number to cause ablation — while for $F < 90\epsilon/\sigma$, the sample remains intact after the reflection of the wave. This thus establishes that the increase of $P_{\min}$ at high fluence is caused by the formation of defects in the surface area of the target. The behavior of $P_{\min}$ is very similar to that observed in simulations of ablation in organic solids (Ref. [66]), except that the peak in the tensile pressure does not coincide with the ablation threshold in our simulations but, rather, corresponds to a damage threshold.

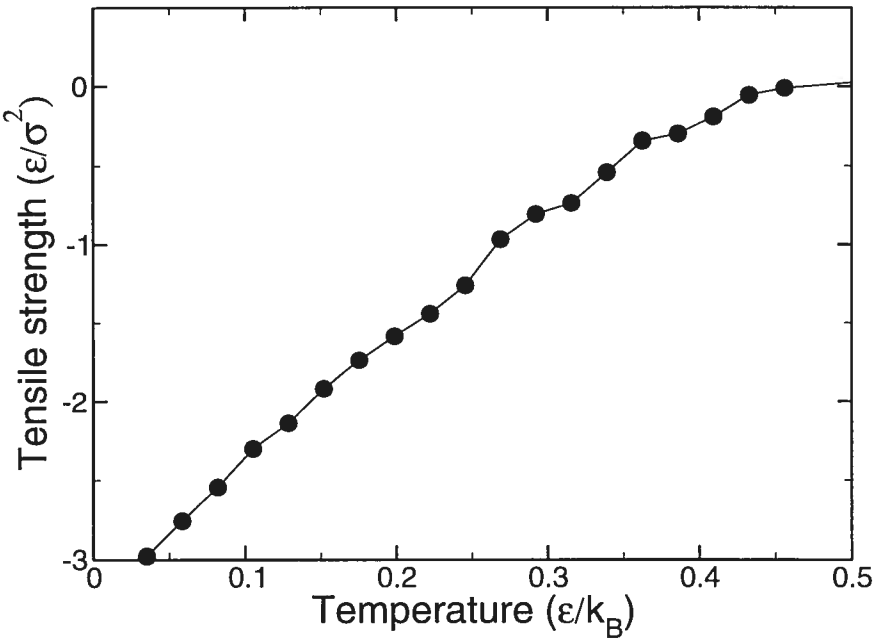

FIG. 2.13 – Tensile strength of the 2D Lennard-Jones solid as a function of temperature.

The fluence at which the tensile wave disappears can be calculated by considering the dependence on temperature of the elastic properties of the material. Indeed, because the tensile component of the pressure wave results from the reflection of the compressive wave on the free surface, P_{min} cannot assume values lower than the tensile strength of the material in the surface region. Following Ref. [14], we consider that the tensile (spall) strength at a given temperature is the minimum pressure reached on the corresponding isotherm. Further stretching of the material along this isotherm would push the material in a region of negative compressibility, where the system is unstable against density fluctuations, hence inducing its failure.

The results, presented in Fig. 2.13, show that the tensile strength is an increasing function of temperature that goes to zero as temperature reaches $0.45\epsilon/k_B$. Thus, if the surface region is hotter than this value during the emission of the compressive waves, the reflection will be completely inelastic and all the energy of the incident wave will be dissipated through the creation of defects. If we require the

tensile strength to vanish at a depth of α^{-1} under the surface to ensure a complete dissipation of the incident compressive wave (remembering that the tensile wave is fully formed only at α^{-1} under the surface), we find that no tensile wave should form for fluences higher than $F = 210\epsilon/\sigma$ at $\alpha = 0.01\sigma^{-1}$. We see from Fig. 2.12 that this fluence corresponds to the beginning of the saturation regime of P_{min}. For fluences higher than this value, the tensile pressure inside the sample is not caused by the passage of an acoustic wave, but results from the expansion speed difference between the solid, nonablated target and the expanding liquid material which induces tension at the interface between the two phases.

We have demonstrated that the formation of tensile pressure waves does not occur at high fluence because of the thermal softening of the material. Thus, tensile-wave-mediated effects play a role in ablation only for fluences around the ablation threshold. The dissipation of the energy contained in the compressive wave incident on the surface will certainly have an impact on the expansion dynamics and on the ejection of material at higher fluences. However, in our simulations, the energy contained in this wave is at most 20% of the total injected energy. The influence of this contribution on the dynamics of the surface regions is thus expected to be modest.

2.3.2 Mechanisms of ablation

It was shown in the preceding sections that different regions form in the target during the ablation process. These regions differ in their expansion dynamics and morphology, and in the thermodynamical relaxation path they follow. This suggests that different ablation mechanisms may be effective in each of these regions. We now demonstrate that it is indeed the case. The thermodynamical trajectories of the different regions of the target indicate that four different ablation mechanisms are present : spallation, homogeneous nucleation, fragmentation and vaporization. They are discussed below in order of increasing energy.

2.3.2.1 Spallation

Spallation is the result of internal failure due to the creation of defects induced by tensile stresses. This phenomenon is routinely observed in ablation experiments on gels [36] and biological tissues. [24] Simulations of ablation of organic solids in the stress-confinement regime have been interpreted in terms of a spallation-like process. [66] In the case of more cohesive solids (metals, semiconductors), the role of the so-called front-side spallation has not yet been clarified. While spallation is sometimes used to describe failure in solids as well as in liquids, we restrict the use of the term to describe the fracture of a solid in which the tensile strength is exceeded. In contrast, the failure of a liquid under tension by nucleation of gas bubbles (while the system is in a metastable state) will be referred to as cavitation, or simply homogeneous nucleation.

In Section 2.3.1.3 it was shown that important tensile waves form at fluences close to the threshold for ablation. Spallation should thus be observable in this regime. Indeed, as shown in Fig. 2.14, ablation proceeds by the ejection of complete layers of material at the threshold fluence. This behavior is very similar to that observed in simulations of ablation of organic solids, [66] in laser-induced back-spallation experiments,[55] and in computer simulations of flyer-plate collisions. [59] In all cases, the passage of a tensile wave induces fractures parallel to the surface of the sample and ejection of complete layers of material. The first snapshot in Fig. 2.14 shows the state of the system at $t = 50\tau$. By then, the tensile wave has already crossed most of the sample and a large number of small pores are visible near the surface. During the next 100τ's they grow and coalesce to finally cause the ejection of the complete surface layer. No voids form very close to the surface because the tensile wave only develops as it travels towards the bulk.[8] The ejected layer eventually breaks up as the expansion continues.

Fig. 2.15 confirms in a quantitative manner that spallation is responsible for ablation in this regime. The trajectories in the $\rho - T$ plane show that absorption of the laser pulse initially heats the slice up to a very high temperature (larger than the critical temperature). However, expansion quickly sets in and lowers the temperature below the triple point after a small incursion into the solid-liquid

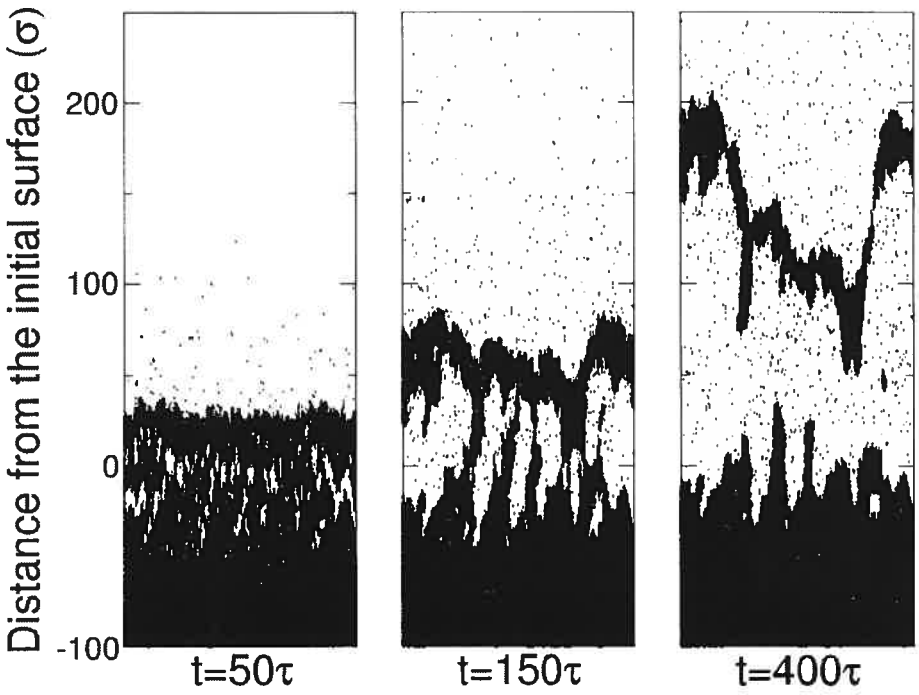

FIG. 2.14 – Snapshot of the system showing ablation by a spallation mechanism; $F = 150\,\epsilon/\sigma$, $\alpha = 0.01\sigma^{-1}$.

coexistence region. The inset shows that the tensile wave reaches this slice when $\rho \simeq 0.81\sigma^{-2}$, then induces further stretching of the material. The split between the average and condensed branches in the $\rho-T$ plane indicates that the material finally fractures around $\rho \simeq 0.76\sigma^{-2}$. After the failure, the temperature rises significantly and the density on the condensed branch increases, indicating that the stretching induced by the passage of the tensile wave causes some of the thermal energy of the slice to be momentarily converted into elastic energy. During the fracture process, part of the stored elastic energy is converted back into heat, causing the observed rise of both temperature and density on the condensed branch. Nevertheless, a decrease of the average density is observed because of the opening of voids. The coalescence of these will later induce ablation.

Following the definition of the tensile strength given in Section 2.3.1.3, failure of the material should occur when the system reaches the minimum pressure of the isotherm on which it lies at this moment. The inset of Fig. 2.15 confirms that this is indeed the case by showing in the $\rho - P$ plane, the average trajectory of the

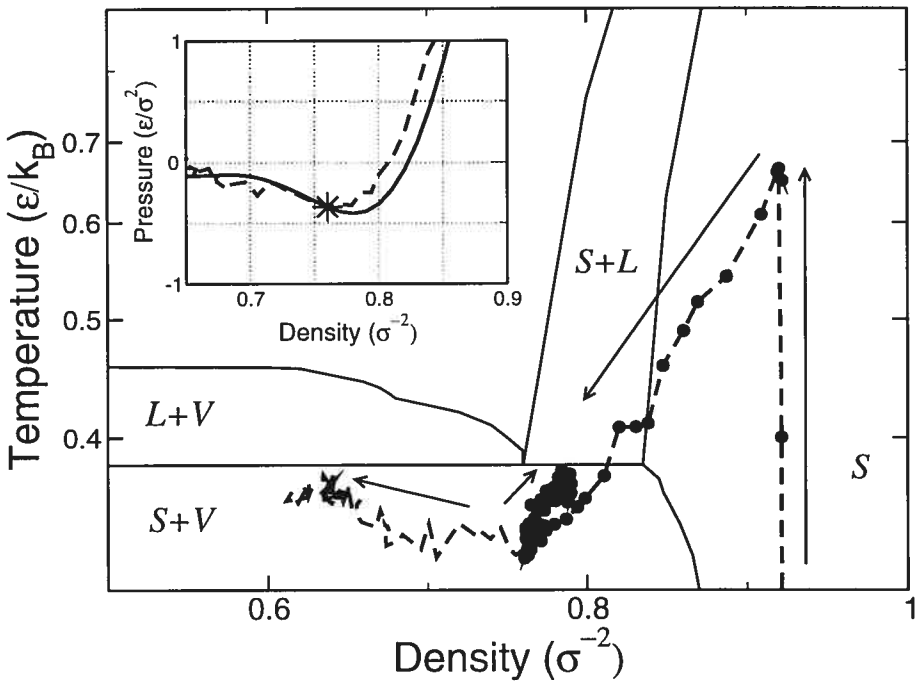

FIG. 2.15 – Typical thermodynamical evolution for regions of the target where spallation occurs, for $F = 150\,\epsilon/\sigma$, $\alpha = 0.01\sigma^{-1}$, $E_{\text{eff}} = 0.95\epsilon/\sigma^2$. Dashed line : average branch ; filled circles : condensed branch. Arrows indicate the flow of time. Inset : average trajectory in the $\rho - P$ plane (dashed line) and $T = 0.36$ isotherm (solid line). The star indicates the point of fracture.

slice together with the $T = 0.36\epsilon/k_B$ isotherm (on which spallation occurs). The failure point is indeed very close to the pressure minimum of this isotherm ; fracture and subsequent ablation are thus caused by the loss of mechanical stability of the expanding system, i.e., again spallation. The pores grow until the stress inside this region is completely relieved.

Spallation in the solid phase was only observed in a small range of fluences around the threshold fluence. Further, "good" stress confinement is required for strong pressure waves to develop ; hence this mechanism is probably restricted to pico and femtosecond pulses. We saw that, as fluence increases, the amplitude of the tensile wave propagating inside the sample decreases and eventually vanishes. As this occurs, the contribution of spallation to the total yield diminishes to the profit of homogeneous nucleation, which we discuss next.

2.3.2.2 Homogeneous nucleation

As seen in Section 2.3.1.2, when higher densities of energy are injected into the system, the relaxation does not proceed within the solid region anymore but, rather, above the triple point : the material melts and later crosses the binodal line, entering the liquid-vapor metastable region of the phase diagram. In this region, the pressure inside the liquid is lower than the saturation vapor pressure. When this occurs, the homogeneous liquid state is no longer the most stable configuration because the free energy of the gas phase becomes lower than that of the liquid.[10] However, the liquid state is still a local free-energy minimum, so an energy barrier has to be crossed for gas domains to nucleate (except at the spinodal line where the barrier vanishes). For long enough waiting times, gas bubbles will thus form inside the liquid through a process called *homogeneous nucleation.*

The decrease of the pressure below the saturated vapor value can be induced by the passage of a tensile wave or simply by adiabatic relaxation during the expansion. If high nucleation rates are reached, ablation can be induced by the rapid transition from a superheated liquid state to a mixture of vapor and liquid droplets through a process referred to as *phase explosion* or *homogeneous boiling.* Since Kelly and Miotello [31, 26, 32] showed that phase explosion is the only thermal mechanism that occurs on a sufficiently small timescale to explain the ejection of liquid droplets in short-pulse experiments, phase explosion is widely considered as the most common cause of ablation in the nano to femtosecond regimes. [31, 26, 32, 62, 61, 7, 50] Phase explosion has also been inferred from the properties of the plume in computer simulations of ablation of organic liquids,[66] but was directly observed only recently in molecular-dynamics simulations by following the thermodynamical evolution of the system.[39] By analogy with liquids, ablation could also possibly occur by hydrodynamic sputtering after the collapse of large bubbles ;[36, 34] this mechanism has however not been observed in the present simulations.

We now show that the growth of gas-filled bubbles in region II of Figs. 2.3 and 2.4 is caused by a homogeneous nucleation process and that ablation follows by homogeneous boiling.

Figure 2.16 shows the thermodynamical signature of a phase explosion process

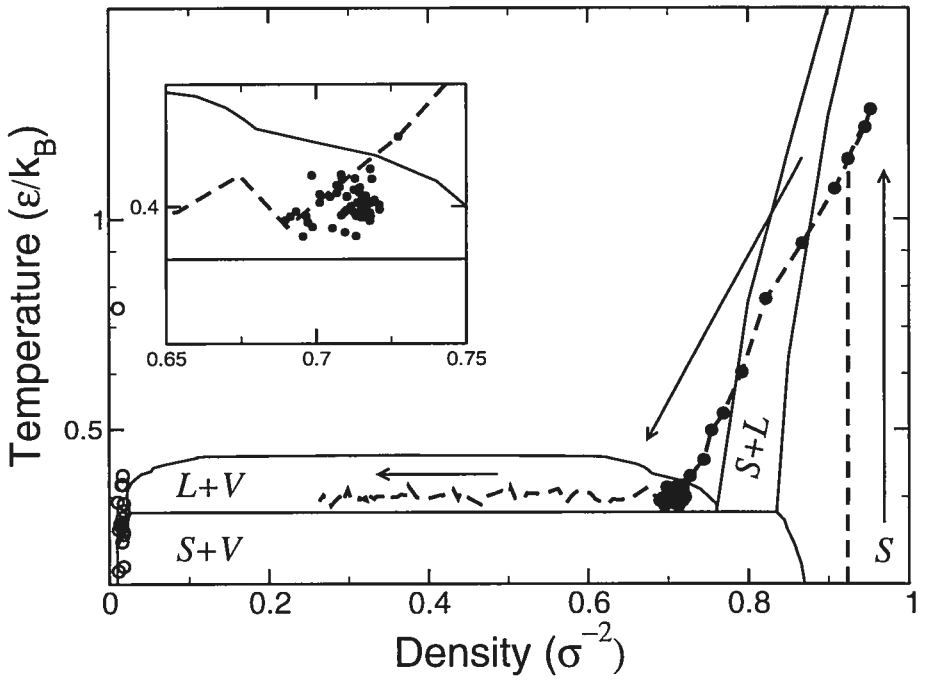

FIG. 2.16 – Typical thermodynamical evolution for regions of the target where homogeneous nucleation occurs, $E_{\text{eff}} = 1.7\epsilon/\sigma^2$. Dashed line : average branch; filled circles : condensed branch; empty circles : gas branch. Inset : zoom on the trajectory at the entrance of the metastable region.

leading to ablation. Once again, the slice is heated at constant volume up to a very high, super-critical temperature. The rarefaction wave then reaches the slice and a quasi-adiabatic relaxation process begins. It proceeds through the solid-liquid coexistence region before the material completely melts upon entering the one-phase liquid region. It can be seen that the system then enters the liquid-vapor metastable region, where the liquid is under tension. Note that no voids are present in the slice before entering the metastable region : the average and condensed branches are completely superimposed. However, the separation of the average and condensed branches, combined with the appearance of the gas branch, confirm that gas-filled bubbles begin to nucleate inside the slice right after the binodal is crossed. A phase separation process then sets in : the condensed phase gradually converts into gas by nucleation and growth of gas regions. However, the timescale for this transformation to take place is very long, so liquid droplets can persist in the plume for a very long time. Because the free-energy barrier for the nucleation

of gas bubbles is very low for any significant incursion into the metastable region (and finally vanishes at the spinodal line),[45] nucleation proceeds at a large rate. The growth and coalescence of these gas-filled bubbles, clearly visible in region II of Figs. 2.3 and 2.4, will eventually cause the ablation of large liquid droplets.

Despite wide acceptance of the mechanism, there is still some confusion in the literature about the conditions in which phase explosion occurs. While it is recognized that a rigorous criterion should be based on the approach of the spinodal line, it is often assumed that a sufficient condition for important density fluctuations and homogeneous nucleation to take place is that the peak temperature inside the target exceeds $T = 0.9\,T_c$. [31, 26, 32, 62, 61, 7] This criterion is correct for slow heating rates at ambient pressure when the system evolves along the binodal line; however, it does *not* apply in stress-confinement conditions typical of short-pulse laser ablation experiments. Indeed, the system can be heated to temperatures higher than T_c but still relax within the solid regions of the phase diagram without ever entering the metastable region (the only region in which homogeneous nucleation is possible). An example of this behavior is given in Fig. 2.15. In fact, the important quantity for the occurrence of phase explosion is the nucleation rate : [46]

$$J = A \exp(-\frac{\Delta G}{k_B T}) \tag{2.5}$$

where A is a kinetic factor that depends weakly on temperature and ΔG is the free-energy barrier for nucleation. [46] As this free-energy barrier vanishes *for all points along the spinodal line*, a temperature close to the critical temperature is not required for significant nucleation to occur; the only condition is to reach deep enough into the metastable region.

In conditions of isochoric heating and adiabatic expansion, phase explosion can occur for relaxation along isentropes intersecting the binodal line between the triple and critical points. Knowledge of the equation of state of the material is then sufficient to compute both these limits and to obtain the energy density interval for which homogeneous nucleation takes place. However, in typical laser ablation experiments, the expansion is non-adiabatic because the emission of pressure waves during the relaxation induces faster-than-adiabatic cooling. The adiabatic hypo-

thesis thus underestimates the energy required for phase explosion to occur.

For good enough thermal confinement, phase explosion can also occur with longer pulses. However, in this case, the material follows a different thermodynamical path than that presented in Fig. 2.16 : expansion occurs during heating as the pulse length is increased until the expansion eventually proceeds along the binodal line for long enough pulses.

As discussed briefly in Ref. [39], our simulations confirm that phase explosion by homogeneous nucleation of bubbles is indeed effective in short-pulse laser irradiation conditions at moderate energies. We will now see that, at higher energies, fragmentation replaces phase explosion as the dominant ablation mechanism.

2.3.2.3 Fragmentation

In a preliminary report of this work, [39] we have shown that fragmentation of a super-critical fluid could account for a significant part of the total ablation yield in short-pulse conditions. We now proceed with a detailed analysis of this mechanism.

Fragmentation is the process whereby an initially homogeneous medium decomposes into a collection of clusters as a result of impact or expansion. This mechanism has been observed in a wide range of systems under large strain rates : continuous systems under adiabatic expansion, [21, 15, 3, 56] ishochoric heating of small droplets, [5, 57, 53] free-jet expansion of liquids ,[28, 4] etc. In laser ablation conditions, photomechanical fragmentation occurs as a result of the conversion of the stress induced by the constant volume heating into strain during the subsequent expansion. [39]

Fragmentation, like homogeneous nucleation, is initiated by thermal fluctuations. If the expansion speed gradient imposed on the sample is small, the local density inhomogeneities induced by the fluctuations are removed by the diffusion of neighboring atoms, thus preserving the equilibrium structure of the fluid. However, for high enough strain rates, diffusion is not sufficient : density inhomogeneities survive and actually grow, resulting in a fragmented-fluid configuration. Fragmentation is thus a strain-induced structural reorganization of a single phase (a supercritical fluid in the present case), in contrast to homogeneous boiling, which implies a change in the balance between two phases. It also differs from spallation because

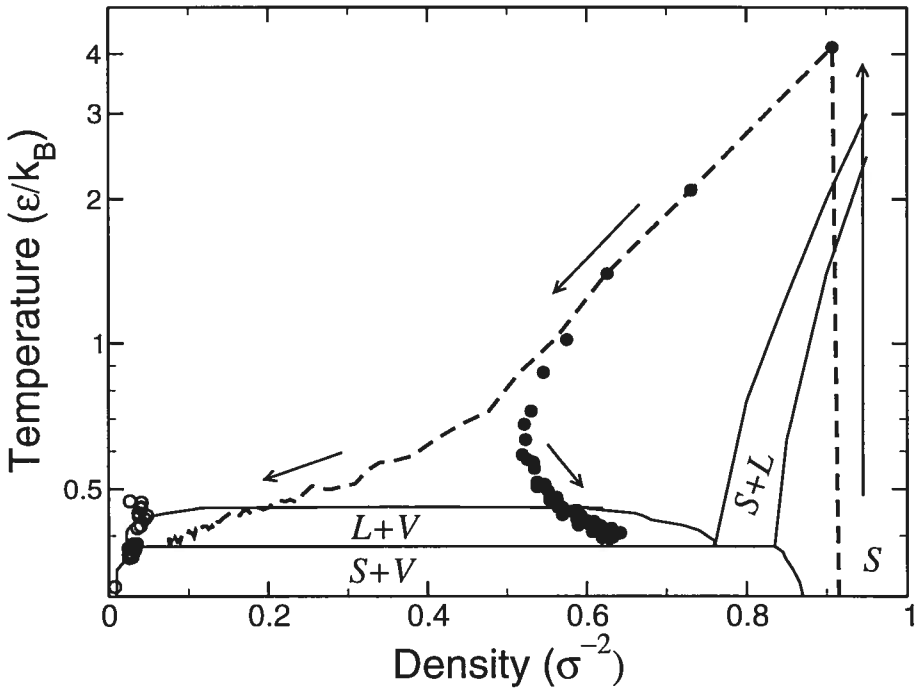

FIG. 2.17 – Typical thermodynamical evolution for regions of the target where fragmentation occurs; $E_{\text{eff}} = 5.4\epsilon/\sigma^2$. See Fig. 2.16 for the definition of symbols and lines.

it does not require the passage of tensile pressure waves in order to occur.

We first demonstrate that ablation in the high-expansion-speed regime (Region III) is not induced by a photo-thermal process; we will then show that fragmentation is responsible for ablation in this case. Figure 2.17 shows the thermodynamical evolution of a slice in this regime. The heating rate is now so intense that the material is pushed into a strongly superheated solid state. Melting occurs at the very beginning of the relaxation and the material then expands in a super-critical fluid state. Soon after, voids begin to appear. The split between the average and condensed branches — indicating the onset of pore creation — now occurs way *above* the binodal line, implying that the system has already decomposed by the time the metastable region is reached. This therefore *excludes* homogeneous nucleation as the mechanism responsible for ablation in this regime. Further, region III of Fig. 2.4 shows that large clusters are present in the plume, so vaporization must also be excluded. Since Kelly and Miotello [32] showed that homogeneous nucleation and vaporization are the only two photo-thermal processes relevant to the description

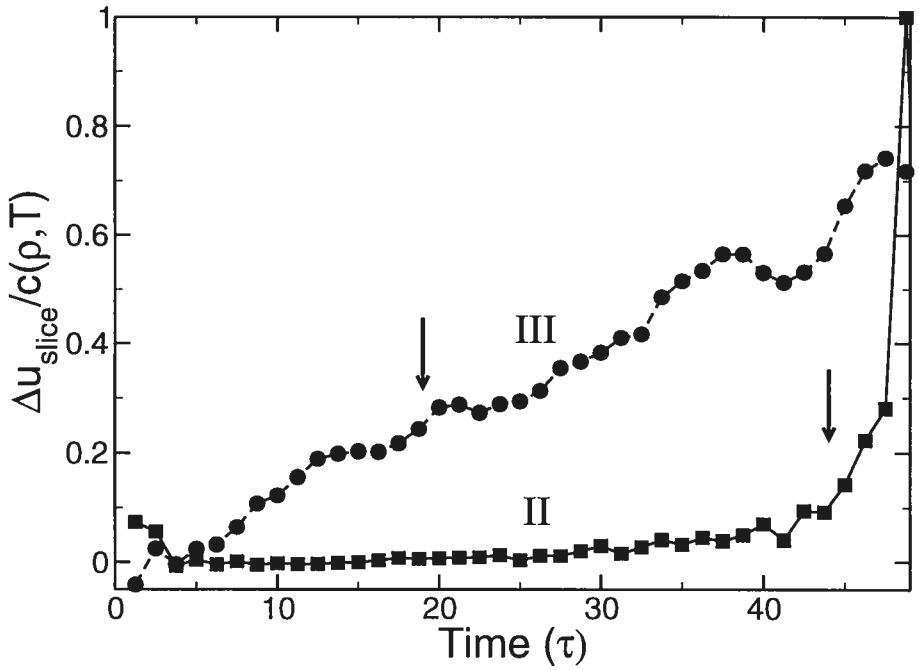

FIG. 2.18 – Ratio of the differential expansion speed within a single slice to the instantaneous speed of sound with $\alpha = 0.01\sigma^{-1}$. Squares : $E_{\text{eff}} = 1.05\epsilon/\sigma^2$ (Region II) ; circles : $E_{\text{eff}} = 3.6\epsilon/\sigma^2$ (Region III). Arrows indicate the onset of void formation.

of ablation in short-pulse conditions, we must therefore conclude that *ablation is not caused by a photo-thermal mechanism* in this regime.

We saw in Section 2.3.1.2 that, in region III, the expansion speed is a strongly dependent function of the injected energy, and hence of the position inside the target. In this case, the exponential heating profile induces very important strain rates ($\eta = \mathrm{d}u/\mathrm{d}y$) and thus creates ideal conditions for the occurrence of fragmentation. This is shown in figure 2.18, where we plot the time dependence of the differential expansion speed between the two ends of a single slice relative to the instantaneous speed of sound. We see that, for expansion in region III (circles), the ratio increases quickly and reaches about a third by the time voids begin to form. As mass transport necessarily occurs at a speed lower than the speed of sound, diffusion will not be efficient enough to balance out anything but the smallest density fluctuations. In this case, the equilibrium structure of the fluid will be lost as new surfaces appear inside the liquid. In contrast, in region II (squares), where the

expansion speed depends only weakly on the injected energy (see Fig. 2.5), the ratio remains very low until the system enters the liquid-vapor metastable region. At this moment, the speed of sound drops abruptly so that the ratio suddenly increases. In this case, the expansion can be considered quasi-static and diffusion preserves the equilibrium structure of the fluid up to the entrance of the metastable region.

Thus, ablation is *not* caused by a photo-thermal process in Region III ; we have also shown that the conditions required for fragmentation are present. We now demonstrate explicitly, through an analysis of the fragment mass distribution of the plume, that fragmentation is indeed responsible for ablation.

A simple model for the fragmentation of continuous systems has been proposed by Ashurst and Holian [3]. In this model, the elastic potential energy ϕ_{elast} stored in the system as a result of expansion is converted into surface energy ϕ_{surf} by a bond-breaking mechanism. In the context of a two-dimensional uniaxial expansion, we have, for a fragment of side L :

$$\phi_{\text{elast}} = \frac{1}{2} B_0 L_0^2 (\eta t)^2, \tag{2.6}$$

where $B_0 = \rho_0 c_0^2$ is the bulk modulus, and :

$$\phi_{\text{surf}} = 4\rho L r_0 \gamma, \tag{2.7}$$

with r the bond length and γ the surface energy density. The subscript 0 indicates quantities evaluated at the beginning of the expansion, while others are evaluated at fragmentation time.

Fragmentation occurs when the elastic energy stored in a region of the target is equal to the surface energy it would have if isolated. At this point, the excess elastic energy is converted into surface energy and fragments are created. Within this model, it can be shown that the mean cluster mass is given by : [3]

$$M = 4\zeta\rho(r_0\gamma)^{2/3}\eta^{-4/3} \tag{2.8}$$

where the geometric factor $\zeta \sim 1$ allows for arbitrary cluster shapes. Equation 2.8

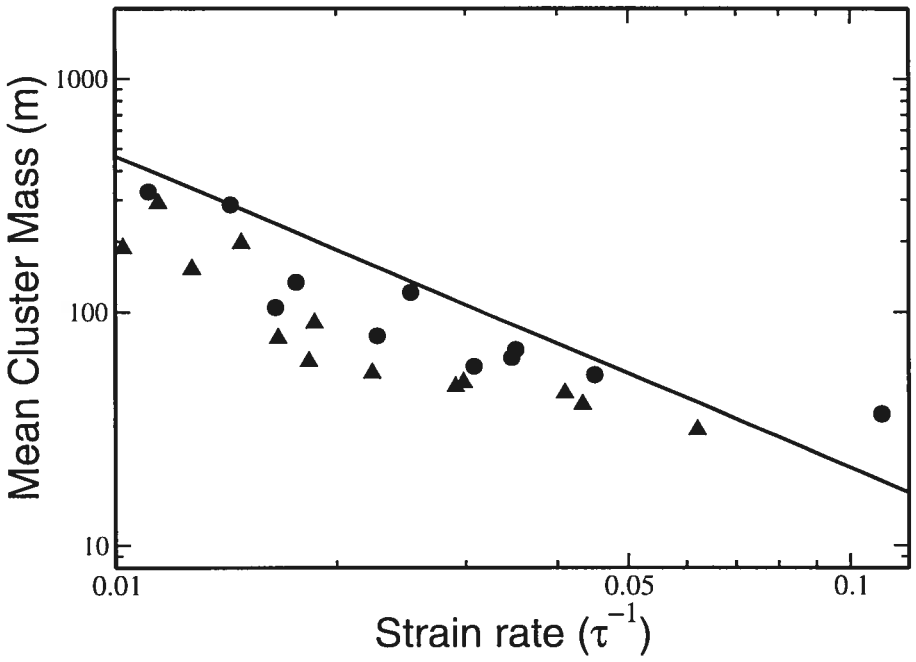

FIG. 2.19 – Mean cluster mass versus local strain rate for $\alpha = 0.01\sigma^{-1}$. Circles : $F = 750\epsilon/\sigma$; triangles : $F = 900\epsilon/\sigma$. The solid line is Eq. 2.8.

expresses the fact that higher strain rates cause more elastic energy to be stored inside the material and hence more energy to be dissipated by the opening of voids. However, equation 2.8 also says that fragmentation does not depend only on the elastic energy stored in the sample (itself a function of the strain) : it also depends explicitly on the speed gradient (strain rate) imposed to the system. Fragmentation is thus a non-equilibrium process and does not occur in the quasi-static expansion limit.[56]

The same scaling law between the size of clusters and the strain rate (but with a different prefactor) can actually be obtained using the Grady model. [18, 5, 3] In this model, the sum of expansion and surface energies is minimized ; for high enough strain rates, the most stable configuration is the fragmented one, i.e., it becomes more energetically favorable for the system to fragment than to continue expanding homogeneously. This scaling-law thus constitutes a strong signature of fragmentation.

We therefore computed the mean mass of clusters as a function of strain rate at their formation depth in the high expansion speed region. This data is shown

in Fig. 2.19 together with the prediction of Eq. 2.8, where we have used $\zeta = \frac{\pi}{4}$ (circular clusters) and $\rho = 0.6\sigma^{-1}$. The surface energy density γ is taken to be the mean energy of a bond at breakup time multiplied by the number of broken bonds per atom. The data clearly reproduce the predicted power law behavior. Further, the prefactor obtained from a fit to the data agrees to within 30% with the one deduced from Eq. 2.8. Given the simple nature of the model, the fit is certainly excellent and clearly indicates that ablation is determined by the expansion rate of the material and is thus caused by fragmentation.

Because the fragmented fluid is not in an equilibrium state, the fragment size distribution evolves in time : if the final state of the average thermodynamical trajectory falls in the one-phase gas region, the clusters will evaporate to restore equilibrium. This is observed in our simulations and explains the presence of many monomers in the fragmented region (cf. region III of Fig. 2.4). Thus, the Ashurst-Holian prediction is valid only at early times because the liquid-gas transition is not bypassed : it occurs from a fragmented state rather than from a homogeneous one. However, the time required for complete equilibration to take place is very long so liquid droplets can survive in the plume for an extended period of time. Hence, the observation of liquid droplets surrounded by monomers in the plume is *not* an indication of phase explosion.

It was shown in section 2.3.1.2 that strongly energy dependent expansion speeds are measured for super-critical relaxations paths. The large strain rates present in the region of the target relaxing along such paths (region III) thus produce ideal conditions for the occurrence of fragmentation. Indeed, all fragmenting trajectories were observed in this regime. A rough estimate of the minimum energy density for which fragmentation occurs is thus given by the energy required for the material to reach the critical point isentrope. However, by contrast with thermal mechanisms, fragmentation does not depend only on the relaxation isentrope, but also on the strain rates induced in the target. As the flow speed is mainly determined by the effective energy, high strain rates will result from large absorption coefficients. In this case, the balance between fragmentation and homogeneous nucleation will tilt in favor of the former : some slices relaxing on isentropes crossing the binodal between

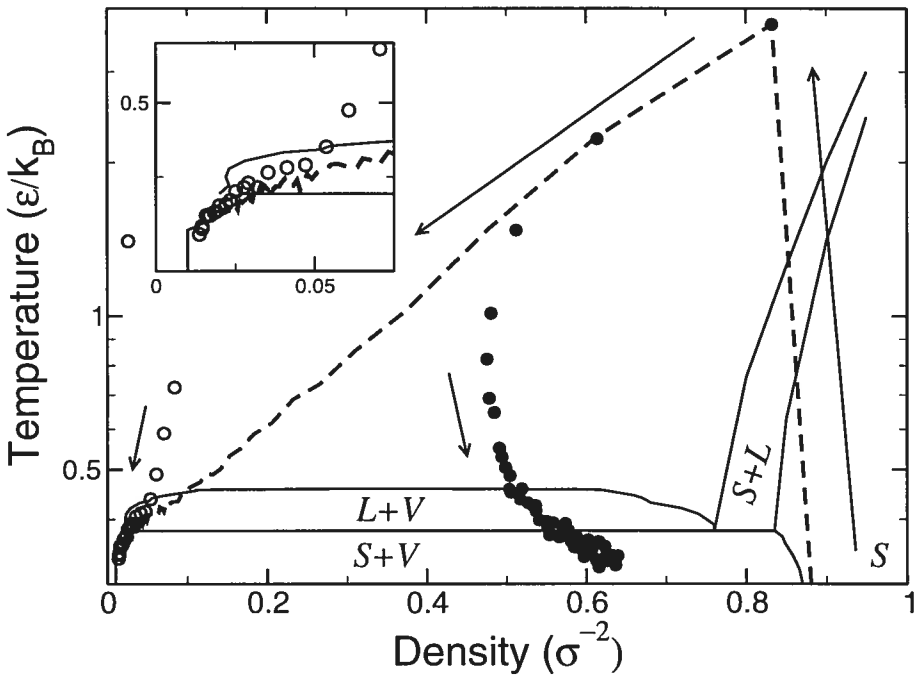

FIG. 2.20 – Typical thermodynamical evolution for regions of the target where vaporization occurs; $E_{\text{eff}} = 7.7\epsilon/\sigma^2$. Inset : enlargement of the low-T-low-ρ region. See Fig. 2.16 for the definition of symbols and lines.

the triple and critical points will fragment before entering the metastable zone. However, at small absorption coefficient, phase explosion will prevail up to the critical point isentrope and fragmentation will be limited to super-critical conditions.

2.3.2.4 Vaporization

At high enough energies, the surface layer of the target is completely atomized and expands at very high speed (cf. part IV of Fig. 2.5). Very few clusters are present in this part of the plume. The evolution of a slice in this regime is presented in Fig. 2.20.

We see from this figure that the condensed and gas branches split at a very early time and that the average and gas branches merge soon after, indicating that the slice as a whole is behaving like a gas. As stated earlier, expansion occurs along perfect-gas-like isentropes in this regime. The trajectory thus simply illustrates a vaporization process. Note that only about 5% of the atoms from the slice are contained in clusters at the end of the simulation so the behavior of the condensed

branch is not very meaningful.

2.3.3 Ablation depth

Armed with the knowledge of the ablation mechanisms identified in the previous section, it is possible to predict, for high enough fluences, the dependence of the ablation depth on fluence, a very important quantity for practical applications.

We showed earlier that the mechanical and thermodynamical evolution of a slice is, in a first approximation, only a function of the effective energy. Away from the threshold fluence, phase explosion is the ablation mechanism requiring the smallest amount of energy. The ablation and phase explosion thresholds should thus be the same : slices which possess effective energies greater than the threshold ($E_{\text{eff}-\text{th}}$) will experience ablation by phase explosion, fragmentation or vaporization, while slices which possess effective energies less than the threshold will relax to a solid state without being ejected. Following the discussion of section 2.3.2.2, $E_{\text{eff}-\text{th}}$ should be given by the energy required to reach the triple point isentrope from the initial state. Since the effective energy density at depth y is approximately given by

$$E_{\text{eff}}(y) = [1 - a(F)]\alpha F e^{-\alpha y} \tag{2.9}$$

where $a(F)$ is the efficiency of the acoustic conversion at this fluence $[a(F) = E_{\text{waves}}(F)/E_{\text{laser}}(F)]$, the depth at which the effective energy is equal to the threshold for ablation is :

$$y(F) = \alpha^{-1} \ln\left(\frac{\alpha F[1 - a(F)]}{E_{\text{eff}-\text{th}}}\right). \tag{2.10}$$

The quantity $a(F)$ was calculated independently as follows : We constructed a sample composed of the usual target on which a very thick layer of the same material was placed. However, this new layer was not allowed to absorb the incoming laser pulse (i.e., is transparent). Pressure-absorbing boundary conditions were applied to both ends of the target, while periodic boundary conditions were used in the x direction. Because the two regions have the same acoustic impedance, the component of the pressure wave that is usually reflected from the free surface of

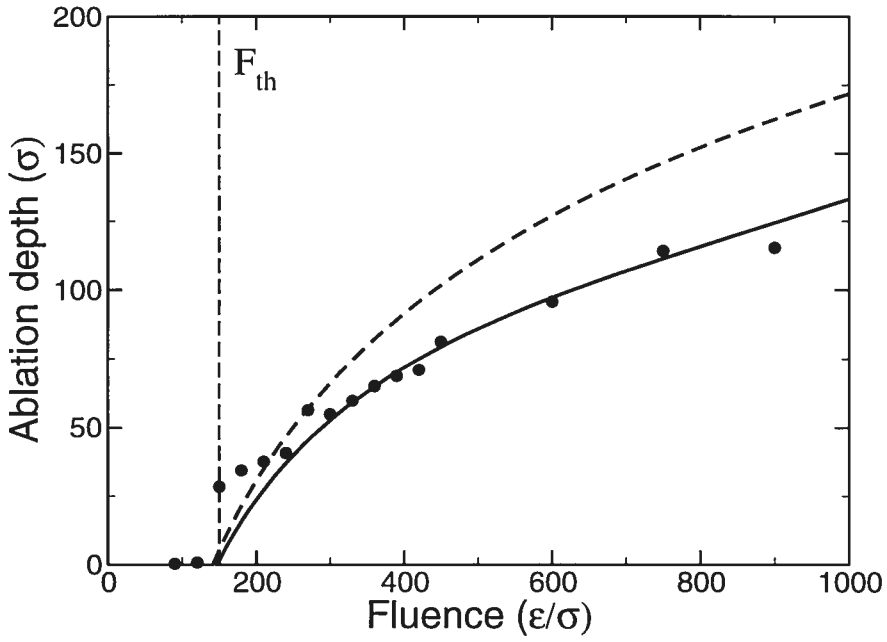

FIG. 2.21 – Ablation depth, $\alpha = 0.01\sigma^{-1}$. Dashed line : Eq. 2.11, Continuous line : Eq. 2.10 with $E_{\text{eff}} = 1.16\epsilon/\sigma^2$.

the absorbing medium after the emission of pressure waves is now transmitted into the transparent material. The other component still proceeds toward the bottom of the sample. The acoustic energy (E_{waves}) is obtained by measuring the drop in the total energy of the system after the absorption of the pressure waves by the special boundary conditions, which can then be divided by E_{laser} to yield a. (One cannot compute E_{waves} with the usual sample, because the reflection of the wave on the free surface is not elastic at high fluences. The acoustic energy collected at the bottom of the sample would thus be less than the initially emitted acoustic energy.)

For comparison, if we neglect the effect of energy loss by the generation of pressure waves, we obtain the well known expression :

$$y(F) = \alpha^{-1} \ln\left(\frac{\alpha F}{(\alpha F)_{\text{th}}}\right) \tag{2.11}$$

In Fig. 2.21 we show a comparison of the data from our simulations with both

expressions. An excellent fit is obtained using Eq. 2.10 with $E_{\text{eff-th}} = 1.16\epsilon/\sigma^2$. This value corresponds to the onset of the phase explosion region (cf. region II of Fig. 2.5 and Section 2.3.2.2). In contrast, Eq. 2.11 overestimates the energy available for ablation and hence the total yield. The cooling induced by the pressure wave formation is thus important enough to notably affect the ejection of atoms from the target.

Note that both expressions underestimate the ablation depth for fluences around the threshold. This discrepancy is due to contributions from spallation effects. Indeed, at the threshold fluence, homogeneous nucleation only occurs within a few slices near the surface but many are ejected following spallation. This proportion gradually increases in favor of homogeneous boiling as the fluence increases. However, it is very difficult to predict the spallation depth because the dynamics of the pressure wave formation in a material with strongly position (temperature) dependent properties is very difficult to estimate. Nevertheless, as the fluence increases, the tensile waves disappear, so phase explosion becomes totally responsible for the onset of ablation and equation 2.10 becomes correct.

The logarithmic variation of the ablation depth with increasing fluence has been reported for the ablation of metals using femtosecond laser pulses [40, 33]. These experiments also show that the typical ablation depths for near-threshold fluences are a few tens of nanometers per pulse, in agreement with our simulations.

2.4 Summary

The ablation of solids under femtosecond laser pulses has been studied using molecular-dynamics simulations. Our calculations show that the reaction of the target is strongly dependent on the energy density injected by the laser through the thermodynamical trajectory by which the matter relaxes. This causes the formation of distinct regions with specific expansion dynamics at different depths under the surface of the target. Temperature variations of the mechanical properties of the target are also shown to cause changes in the shape of the generated pressure waves; from bipolar at low fluence to unipolar at high fluence. This implies that tensile-wave-mediated effects are only effective at low fluences. Indeed, spallation

is only observed when the tensile component of the pressure wave is sufficiently important. Phase explosion is the main mechanism responsible for ablation at moderates fluences. This mechanism occurs in slowly-expanding regions of the target and is able to produce conditions in which Newton rings are expected to form. For high strain rates, the plume is formed by mechanical fragmentation of the expanding medium. Complete vaporization of the surface layers is also observed. These mechanisms typically occur simultaneously at different positions under the surface of the target. Finally, a formula for the ablation depth is presented and it is shown that the pressure waves formation must be considered in order to predict the ablation yield correctly.

We thank Patrick Lorazo, Ralf Meyer and Michel Meunier for numerous enlightening discussions. This work has been supported by grants from the Canadian *Natural Sciences and Engineering Research Council* (NSERC) and and Québec's *Fonds québécois de la recherche sur la nature et les technologies* (NATEQ). We are indebted to the *Réseau québécois de calcul de haute performance* (RQCHP) for generous allocations of computer resources.

CONCLUSION

Le phénomène d'ablation laser par impulsions ultra-courtes a été étudié à l'aide d'un modèle de dynamique moléculaire en deux dimensions. L'analyse des résultats a été orientée vers les aspects mésoscopiques du problème, i.e., la description de la réaction globale de la cible après l'irradiation laser ainsi que l'identification des mécanismes responsables de l'éjection de matière.

Dans le cadre du premier volet de l'étude, notre attention s'est portée sur la dynamique d'expansion de la cible et sur le processus de génération d'ondes de choc lors de la relaxation du système. Les résultats montrent que différents régimes d'expansion se forment à l'intérieur de la cible en fonction de l'énergie injectée par le laser. L'origine de ces régimes repose sur des différences importantes dans la forme des isentropes le long desquelles l'expansion a lieu. En effet, l'expansion de la matière relaxant par des trajectoires thermodynamiques qui entrent dans les regions de coexistence solide-vapeur et liquide-vapeur s'effectue à vitesse faible. De plus, la vitesse d'expansion est faiblement dépendante de l'énergie injectée dans ces régimes. Ce comportement est radicalement modifié lorsque le chauffage causé par l'absorption de l'impulsion laser est suffisant pour induire une relaxation supercritique. Dans ce dernier cas, l'expansion est rapide et fortement dépendante de l'énergie injectée, imposant de forts taux d'étirement (*strain rates*) au matériau. Les ondes de pression générées par la relaxation du fort gradient de pression thermoélastique subissent aussi des changements importants lorsque la fluence augmente : la forme bipolaire du profil de pression à basse fluence devient unipolaire à haute fluence. Cette transformation découle de la perte de résistance tensile du solide à haute température. Ce résultat indique que les effets mécaniques induits par le passage d'ondes tensiles sont limités au régime de basse fluence.

Le deuxième et principal volet de notre étude concerne l'identification et la caractérisation des différents processus d'ablation. En couplant les résultats obtenus précédemment avec une analyse des trajectoires thermodynamiques des différentes parties de l'échantillon, quatre mécanismes d'ablation ont pu être identifiés. Le premier est la spallation. Ce mécanisme cause l'éjection d'agrégats solides suite

à des fractures induites par le passage d'ondes tensiles. Conformément à ce qui a été expliqué plus haut, ce mécanisme n'est observé qu'à l'intérieur d'une faible bande de fluences près du seuil d'ablation. Pour des fluences légèrement supérieures au seuil, les trajectoires thermodynamiques montrent que l'explosion de phase est responsable de la plus grande partie de l'ablation. Celle-ci est alors causée par la transition rapide d'un liquide surchauffé vers mélange de goutelettes liquides et de vapeur suite à l'entrée du système dans la région métastable liquide-vapeur. À des énergies suffisantes pour induire une relaxation super-critique, l'ablation se produit par un processus de fragmentation. Dans ce cas, la structure d'équilibre du fluide est perdue suite à la formation de gradients de vitesse d'expansion importants qui réduisent l'efficacité des processus de diffusion. Ce mécanisme est proposé ici pour la première fois dans le contexte de l'ablation laser. Finalement, nous avons aussi observé de l'ablation par vaporisation. Les résultats montrent que plusieurs de ces mécanismes peuvent être présents simultanément à différentes profondeur dans la cible.

Bien que nous ayons fait l'hypothèse que seul un mécanisme linéaire (impliquant un seul photon) soit responsable de l'absorption de la lumière, c.-à-d. que le profil de dépôt d'énergie dans la cible soit exponentiellement décroissant, l'analyse de nos résultats indique que la validité de nos conclusions n'en dépend pas de manière importante. En effet, nous avons montré que le facteur décisif déterminant l'évolution d'une région de la cible est la densité d'énergie absorbée localement, puisque cette quantité détermine à son tour l'isentrope le long de laquelle la relaxation du système s'effectue et donc le mécanisme par lequel cette portion de matériau est éjectée (le cas échéant). L'ajout d'autres processus d'absorption de la lumière — l'absorption à deux photons par exemple est habituellement non négligeable en régime femtoseconde — viendrait, bien sûr, modifier le profil de dépôt d'énergie, mais il n'y a pas de raison de croire que ceci induirait de nouveaux mécanismes d'ablation (en autant que ce changement ne cause pas l'apparition d'effets non thermiques importants, comme une ionisation significative de la surface de la cible). Un tel changement pourrait par contre avoir pour effet d'augmenter l'importance relative d'un mécanisme particulier sans toutefois invalider nos conclusions.

Malgré l'atteinte de nos objectifs initiaux, plusieurs questions restent en suspens. Par exemple, il serait intéressant d'étudier comment la dynamique d'expansion de la cible est modifiée par l'allongement de l'impulsion laser incidente et de déterminer de quelle manière les mécanismes d'ablation sont affectés par une baisse de qualité des confinements mécanique et thermique. On pourrait aussi étudier la morphologie des cratères d'ablation produits à l'aide de différents profils de déposition d'énergie, étude très intéressante pour des applications en micro-usinage par exemple. Cependant, dans ce cas, la mise au point d'un modèle en trois dimensions pourrait être requis, puisqu'une comparaison quantitative avec l'expérience serait recherchée. De plus, une attention particulière devrait être portée aux conditions aux frontières, car l'usage de conditions périodiques ne serait plus possible puisque les ondes de pression produites ne se progageraient plus parallèlement au laser et donc ne pourraient pas être absorbées adéquatement à l'aide de la méthode utilisée dans le présent modèle.

BIBLIOGRAPHIE

[1] M.P. Allen and D.J. Tildesley. *Computer Simulation of Liquids.* Oxford Science Publications, Oxford, 1987.

[2] S.I. Anisimov, N.A. Inogamov, A.M. Oparin, B. Rethfeld, M. Ogawa, and V.E. Fortov. Pulsed laser evaporation : equation-of-state effects. *Journal of Applied Physics*, 69 :617–620, 1999.

[3] Wm. T. Ashurst and B. L. Holian. Droplet formation by rapid expansion of a liquid. *Physical Review E*, 59 :6742–6752, 1999.

[4] Wm. T. Ashurst and B. L. Holian. Droplet size dependance upon volume expansion rate. *Journal of Chemical Physics*, 111 :2842–2843, 1999.

[5] J. A. Blink and W. G. Hoover. Fragmentation of suddenly heated liquids. *Physical Review A*, 32 :1027–1035, 1985.

[6] Oleg V. Borisov, Richard E. Russo, and Christopher J. Bannochie. Laser ablation inductively coupled plasma mass spectrometry of pressed pellet surrogates for pu materials disposition. *Applied Spectroscopy*, 55 :1304, 2001.

[7] N.M. Bulgakova and A.V. Bulgakov. Pulsed laser ablation of solids : transition from normal vaporization to phase explosion. *Applied Physics A*, 73 :199, 2000.

[8] J. C. Bushnell and D. J. McCloskey. Thermoelastic stress production in solids. *Journal of Applied Physics*, 39 :5541–5546, 1968.

[9] J.P. Callan, A.M.-T. Kim, C.A.D. Roeser, and E. Mazur. Universal dynamics during and after ultrafast laser-induced semiconductor-to-metal transitions. *Physical Review B*, 64 :073201, 2001.

[10] Van P. Carey. *Liquid-vapor phase-change phenomena.* Hemisphere Pub. Corp., Washington, D.C., 1992.

[11] A. Cavalleri, K. Sokolowski-Tinten, J. Bialkowski, M. Schreiner, and D. von der Linde. Femtosecond melting and ablation of semiconductors studied with time of flight mass spectroscopy. *Journal of Applied Physics*, 85 :3301, 1999.

[12] A. Cavalleri, Cs. Tóth, C. W. Siders, J. A. Squier, F. Ráksi, P. Forget, and J. C. Kieffer. Femtosecond structural dynamics in VO_2 during an ultrafast solid-solid phase transition. *Physical Review Letters*, 87 :237401, 2001.

[13] B. N. Chichkov, C. Momma, S. Nolte, F. von Alvensleben, and A. Tünnermann. Femtosecond, picosecond and nanosecond laser ablation of solids. *Appled Physics A*, 63 :109–115, 1996.

[14] E. Dekel, S. Eliezer, Z. Henis, E. Moshe, A. Ludmirsky, and I.B. Goldberg. Spallation model for the high strain rates range. *Journal of Applied Physics*, 84 :4851, 1998.

[15] C. O. Dorso and A. Strachan. Onset of fragment formation in periodic expanding systems. *Physical Review B.*, 54 :236–243, 1996.

[16] J. I. Etcheverry and M. Mesaros. Molecular dynamics simulation of the production of acoustic waves by pulsed laser irradiation. *Physical Review B*, 60 :9430, 1999.

[17] K. Furusawa, K. Takahashi, H. Kumagai, K. Midorikawa, and M.Obara. Ablation characteristics of au, ag,andcu metals using a femtosecond ti :sapphire laser. *Applied Physics A*, A69 :S359, 1999.

[18] D. E. Grady. Local inertial effects in dynamic fragmentation. *Journal of Applied Physics*, 51 :322–325, 1981.

[19] J.S. Graves and R.E. Allen. Response of gaas to fast intense laser pulses. *Physical Review B*, 58 :13 627, 1998.

[20] R.F.W. Herrmann, J. Gerlach, and E.E.B. Campbell. Ultrashort pulse laser ablation of silicon : an md simulation study. *Applied Physics A*, 66 :35–42, 1998.

[21] B.L. Holian and D. E. Grady. Fragmentation by Molecular Dynamics : The Microscopic "Big Bang". *Physical Review Letters*, 60 :1355, 1988.

[22] J. Hoshen and R. Kopelman. Percolation and cluster distribution. i. cluster multiple labeling technique and critical concentration algorithm. *Physical Review B*, 14 :3438–3445, 1976.

[23] N.A. Inogamov, S.I. Anisimov, and B. Retfeld. Rarefaction wave and gravitational equilibrium in a two-phase liquid-vapor medium. *Journal of Experimental and Theoretical Physics*, 88 :1143–1150, 1999.

[24] I. Itzkan, D. Albagli, M.L. Dark, L.T. Perelman, C. von Rosenberg, and M.S. Fields. The thermoelastic basis of short pulsed laser ablation of biological tissues. *Proc. Natl. Acad. Sci. USA*, 92 :1960, 1995.

[25] A. Kaiser, B. Rethfeld, M. Vicanek, and G. Simon. Microscopic processes in dielectrics under irradiation by subpicosecond laser pulses. *Physical Review B*, 61 :11 437, 2000.

[26] R. Kelly and A. Miotello. Comments on explosive mechanisms of laser sputtering. *Applied Surface Science*, 96 :205–215, 1995.

[27] R. Kelly and A. Miotello. Comments on explosive mechanisms of laser sputtering. *Applied Surface Science*, 96-98 :205–215, 1996.

[28] E. L. Knuth and U. Henne. Average size and size distribution of large droplets produced in a free-jet expansion of a liquid. *Journal of Chemical Physics*, 110 :2664–2668, 1999.

[29] F. Korte, S. Nolte, B.N. Chichkov, T. Bauer, G. Kamlage, T. Wagner, C. Fallnich, and H. Welling. Far-field and near-field material processing with femtosecond laser pulses. *Applied Physics A*, A69 :S7, 1999.

[30] L.D. Landau and E.M. Lifshits. *Course of Theoretical Physics VI : Fluid Mechanics*. Pergamon Press, Oxford, 1982.

[31] A. Miotello and R. Kelly. Critical assessment of thermal models for laser sputtering at high fluences. *Applied Physics Letters*, 67 :3535, 1995.

[32] A. Miotello and R. Kelly. Laser-indiced phase explosion : new physical problems when a condensed phase approaches the thermodynamic critical temperature. *Applied Physics A*, 69 :S69–S73, 1999.

[33] S. Nolte, C. Momma, H. Jacobs, A. Tünnermann, B.N. Chichkov, B. Wellegehausen, and H. Welling. Ablation of metals by ultrashort laser pulses. *J. Opt. Soc. Am. B*, 14 :2716, 1997.

[34] A.A. Oraevsky, S.L. Jacques, and F.K. Tittel. Mechanisms of laser ablation for acqueous media irradiated under confined-stress conditions. *J. Appl. Phys*, 78 :1281, 1995.

[35] A.A. Oraevsky, S.L. Jacques, and F.K. Tittel. Mechanisms of laser ablation for aqueous media irradiated under confined-stress conditions. *Journal of Applied Physics*, 78 :1281–1290, 1995.

[36] G. Paltauf and H. Schmidt-Kloiber. Microcavity dynamics during laser-induced spallation of liquids and gels. *Applied Physics A*, 62 :303–311, 1996.

[37] A. Z. Panagiotopoulos. Direct determination of phase coexistence properties of fluids by monte carlo simulation in a new ensemble. *Molecular Physics*, 61 :813, 1998.

[38] W.S. Pelouch, P.P. van Saarloos, G. Dair, D.J. Lloyd, and S Paz. Results of corneal ablation by ultraviolet 213-nm laser pulses. *The Association for Research in Vision and Ophthalmology*, 39 :S69, 1998.

[39] D. Perez and L. J. Lewis. Ablation of solids under femtosecond laser pulses. *Physical Review Letters*, 89 :255504, 2002.

[40] S. Preuss, A.Demchuk, and M. Stuke. Sub-picosecond uv laser ablation of metals. *Appl. Phys. A*, 61 :33, 1995.

[41] B. Rethfeld, K. Sokolowski-Tinten, and D. von der Linde. Ultrafast melting of laser-excited solids by homogeneous nucleation. *Physical Review B*, 65 :092103, 2002.

[42] A. V. Rode, E. G. Gamaly, B. Luther-Davies, B. T. Taylor, J. Dawes, A. Chan, R. M. Lowe, and P. Hannaford. Subpicosecond laser ablation of dental enamel. *Journal of Applied Physics*, 92 :2153, 2002.

[43] A. Rousse, C. Rischel, S. Fourmaux, I. Uschmann, S. Sebban, G. Grillon, Ph. Balcou, E. Förster, J.P. Geinder, P. Audebert, J.C. Gauthier, and D. Hulin. Non-thermal melting in semiconductors measured at femtosecond resolution. *Nature*, 410 :65–68, 2001.

[44] H. Schäfer, A. E. Mark, and W. F. van Gunsteren. Absolute entropies from molecular dynamics simulation trajectories. *Journal of Chemical Physics*, 113 :7809, 2002.

[45] V. K. Shen and P. G. Debenedetti. Density-functional study of homogeneous bubble nucleation in the stretched lennard-jones fluid. *Journal of Chemical Physics*, 114 :4149–4159, 2001.

[46] V.K. Shen and P.G. Debenedetti. A computational study of homogeneous liquid-vapor nucleation in the Lennard-Jones fluid. *Journal of Chemical Physics*, 111 :3581, 1999.

[47] B. Smit and D. Frenkel. Vapor-liquid equilibria of the two-dimensional Lennard-Jones fluid(s). *Journal of Chemical Physics*, 94 :5663–5668, 1991.

[48] K. Sokolowski-Tinten. Communication privée.

[49] K. Sokolowski-Tinten, J. Bialkowski, M. Boing, A. Cavalleri, and D. von der Linde. Thermal and nonthermal melting of gallium arsenide after femtosecond laser excitation. *Physical Review B*, 58 :11 805, 1998.

[50] K. Sokolowski-Tinten, J. Bialkowski, A. Cavalleri, D. von der Linde, A. Oparin, J. Meyer ter Vehn, and S.I. Anisimov. Transient states of matter during short pulse laser ablation. *Physical Review Letters*, 81 :224–227, 1998.

[51] R. Stoian, A. Rosenfeld, D. Ashkenasi, I. V. Hertel, N. M. Bulgakova, and E. E. B. Campbell. Surface charging and impulsive ion ejection during ultrashort pulsed laser ablation. *Physical Review Letters*, 88 :097603, 2002.

[52] A. Strachan, T. Çağin, and W. A. Goddard III. Critical behavior in spallation failure of metals. *Physical Review B.*, 63 :060103, 2001.

[53] A. Strachan and C. O. Dorso. Caloric curve in fragmentation. *Phys. Rev. C.*, 58 :R632, 1998.

[54] A Strachan and C.O. Dorso. Temperature and energy partition in fragmentation. *Physical Review C*, 59 :285–294, 1999.

[55] H. Tamura, T. Kohama, K. Kondo, and M. Yoshida. Femtosecond-laser-induced spallation in aluminum. *Journal of Applied Physics*, 89 :3520, 2001.

[56] S. Toxvaerd. Fragmentation of fluids by molecular dynamics. *Phys. Rev. E*, 59 :6742, 1999.

[57] A. Vicentini, G. Jacucci, and V.R. Pandharipande. Fragmentation of hot classical drops. *Phys. Rev. C.*, 31 :1783, 1985.

[58] F. Vidal, T.W. Johnston, S. Laville, O. Barthélemy, M. Chaker, B. Le Drogoff, J. Margot, and M. Sabsabi. Critical-point phase separation in laser ablation of conductors. *Physical Review Letters*, 86 :2573–2576, 2001.

[59] N.J. Wagner, B.L. Holian, and A.F. Voter. Molecular-dynamics simulations of two-dimensional materials at high strain rates. *Physical Review A*, 45 :8475, 1992.

[60] P. R. Willmott and J. R. Huber. Pulsed laser vaporization and deposition. *Reviews of Modern Physics*, 72 :315, 2000.

[61] J.H. Yoo, S.H. Jeong, R. Grief, and R.E. Russo. Explosive change in crater properties during high power nanosecond laser ablation of silicon. *Journal of Applied Physics*, 88 :1638, 2000.

[62] J.H. Yoo, S.H. Jeong, X.L. Mao, R. Grief, and R.E. Russo. Evidence for phase-explosion and generation of large particles during high power nanosecond laser ablation of silicon. *Applied Physics Letters*, 76 :783, 1999.

[63] V.V. Zhakhovskii, K. Nishiara, S.I. Anisimov, and N.A. Inogamov. Molecular-dynamics simulations of rarefaction waves in media that can undergo phase transitions. *JETP Letters*, 71 :167, 2000.

[64] V.V. Zhakhovskii, K. Nishihara, S.I. Anisimov, and N.A. Inogamov. Molecular-dynamics simulation of rarefaction waves in media that can undergo phase transition. *JETP Letters*, 171 :167–172, 2000.

[65] L. V. Zhigilei and B. J. Garrison. Pressure waves in microscopic simulations of laser ablation. *Mat. Res. Soc. Symp. Proc.*, 538 :491, 1999.

[66] L. V. Zhigilei and B. J. Garrison. Microscopic mechanisms of laser ablation of organic solids in the thermal and stress confinement irradiation regimes. *Journal of Applied Physics*, 88 :1281–1298, 2000.

[67] X. Zhu, A.Yu. Naumov, D.M. Villeneuve, and P.B. Corkum. Influence of laser parameters and material properties on micro drilling with femtosecond laser pulses. *Applied Physics A*, 69 :S367, 1999.

Annexe I

Dynamique moléculaire

Comme indiqué dans les chapitres 1 et 2, le modèle utilisé lors de nos simulations a été implémenté sous forme d'un programme de dynamique moléculaire (**DM**) [1] en deux dimensions. Puisque la DM est une technique bien connue du milieu de la recherche, sa description a été omise lors de la rédaction des articles présentés dans le corps du mémoire. Dans le but de faire de ce mémoire un tout cohérent, nous présentons ici une brève explication des principes de cette méthode.

I.1 Méthode

La DM consiste essentiellement en l'intégration des équations du mouvement classiques pour un système de N atomes interagissant par un potentiel interatomique $\mathcal{V}$. (Comme mentionné dans le corps du mémoire, le potentiel interatomique choisi dans le cadre de cette étude est le potentiel de Lennard-Jones). On peut dériver ces équations à partir du Lagrangien du système :

$$\mathcal{L} = \mathcal{K} - \mathcal{V} \tag{I.1}$$

À l'aide de la définition standard de l'énergie cinétique

$$\mathcal{K} = \sum_{i=1}^{N} \frac{p^2}{2m} \tag{I.2}$$

et de l'équation du mouvement Lagrangienne

$$\frac{\mathrm{d}}{\mathrm{dt}}\left(\frac{\partial \mathcal{L}}{\partial \dot{\mathbf{q}}_i}\right) - \left(\frac{\partial \mathcal{L}}{\partial \mathbf{q}_i}\right) = 0 \tag{I.3}$$

on obtient en coordonnés cartésiennes :

$$m_i \ddot{x}_i = -\nabla_i \mathcal{V} = f_i \tag{I.4}$$

Cette dernière équation est intégrée numériquement pour donner la trajectoire de la particule dans l'espace des phases. Le schéma d'intégration utilisé est l'algorithme de *Verlet vitesse*. Cet algorithme est de type "leap-frog" car il s'effectue en deux temps. Premièrement, les positions au temps $t + \delta t$ sont évaluées avec

$$x_i(t + \delta t) = x_i(t) + \delta t v_i(t) + \frac{1}{2}\delta t^2 a_i(t) \tag{I.5}$$

Les vitesses à mi-pas sont aussi obtenues par

$$v_i(t + \frac{1}{2}\delta t) = v_i(t) + \frac{1}{2}\delta t a_i(t) \tag{I.6}$$

Ceci vient compléter la première étape de l'intégration des équations du mouvement. Les forces au temps $t + \delta t$ sont ensuite calculées à l'aide des nouvelles positions. Le pas se complète finalement par le calcul des vitesse finales à l'aide de la relation :

$$v_i(t + \delta t) = v_i(t + \frac{1}{2}\delta t) + \frac{1}{2}\delta t a_i(t + \delta t) \tag{I.7}$$

Cet algorithme d'ordre 2 ($\langle \delta \mathcal{H}^2 \rangle^{1/2} \propto \delta t^2$) est très rapide et consomme peu de mémoire. Comme les fluctuations de l'énergie sont proportionnelles à δt^2, l'algorithme de Verlet vitesse permet l'utilisation de longs pas de temps, ce qui en fait un choix très populaire.

I.2 Implémentation

Bien que la DM soit conceptuellement très simple, une implémentation naïve de la méthode est extrêmement inefficace d'un point de vue numérique dès que le nombre d'atomes en jeu, N, devient important. En effet, comme l'ensemble des forces exercées par les atomes entre eux doit être déterminé à chaque pas d'intégration, le temps requis pour calculer ceci à l'aide d'une double boucle (une boucle sur tous les voisins potentiels pour chacun des atomes de la simulation) est proportionnel à N^2. Une solution est de garder en mémoire une liste de tous les voisins d'un atome donné. La boucle de calcul des forces est donc maintenant effectuée en un temps $O(N)$. Cependant, la construction de ces listes de voisins

doit être recommencée périodiquement pour permettre à de nouveaux voisins de s'y inclure et pour permettre aux atomes qui se sont éloignés d'en être éliminés. Cette étape requiert par contre toujours un temps $O(N^2)$, mais n'est pas effectuée à chaque itération. La construction de cette liste peut aussi être optimisée en divisant au préalable la super-cellule de simulation en plus petites cellules. On classe ensuite les atomes selon leur cellule d'appartenance, opération nécessitant une seule passe à travers la liste des atomes. La liste des voisins peut maintenant être construite en cherchant les voisins d'un atome donné seulement à travers sa cellule et ses voisines. Le temps total de calcul est donc maintenant proportionnel aux nombre d'atomes et non plus au carré de ce nombre. Bien que toutes les opération de gestion des cellules et des listes de voisins consomment des cycles de calcul, cette surcharge est amplement amortie par les gains enregistrés au moment du calcul des forces, et ce même pour des petits nombre d'atomes ($N \simeq 1000$). Pour plus de détails sur l'implémentation efficace de programmes de DM, on peut consulter la référence [1].

Annexe II

Propriétés thermodynamiques du potentiel de Lennard-Jones

Pour être en mesure de tirer profit de la méthode de calcul des propriétés thermodynamiques locales, le diagramme de phase du potentiel utilisé doit être bien connu. Bien que le potentiel LJ soit très populaire, les calculs présentés dans la littérature sont habituellement effectués dans la limite d'une portée d'interaction infinie. Comme l'effet de la troncature de la queue à longue portée du potentiel se fait fortement ressentir sur le diagramme de phase, certains calculs ont dû être effectués pour complémenter la faible quantité de données déjà publiées. La présente annexe décrit les méthodes utilisées pour réaliser ces calculs.

II.1 Diagramme de phase

Dans le cas qui nous occupe ici, il est primordial de connaître la position de la binodale (courbe de coexistence liquide-vapeur) dans le diagramme de phase pour pouvoir confirmer ou infirmer l'occurence de l'explosion de phase. Ce calcul a été réalisé en partie par Smit et al.[47], mais les données publiées par ceux-ci n'incluent pas la section à basse température de cette courbe. Des calculs Monte Carlo dans l'ensemble de Gibbs ont donc été effectués pour compléter ces données.

II.1.1 Monte Carlo dans l'ensemble de Gibbs

La méthode Monte Carlo dans l'ensemble de Gibbs [37] a pour objectif de simuler la coexistence de deux phases (I et II) à l'équilibre à une température T. Pour ce faire, deux boîtes sont utilisées : la première contient N^I particules dans un volume V^I et la deuxième N^{II} particules dans un volume V^{II}. Des conditions aux frontières périodiques sont utilisées pour chaque boîte, de sorte que l'interface entre les phases n'est pas modélisé. Comme le nombre total d'atomes, $N = N^I + N^{II}$, ainsi que le volume total, $V = V^I + V^{II}$, sont conservés, et comme la température du système est fixe, le système total évolue dans l'ensemble canonique. La figure II.1 illustre les trois types de mouvements possibles au cours d'une simulation : déplacement

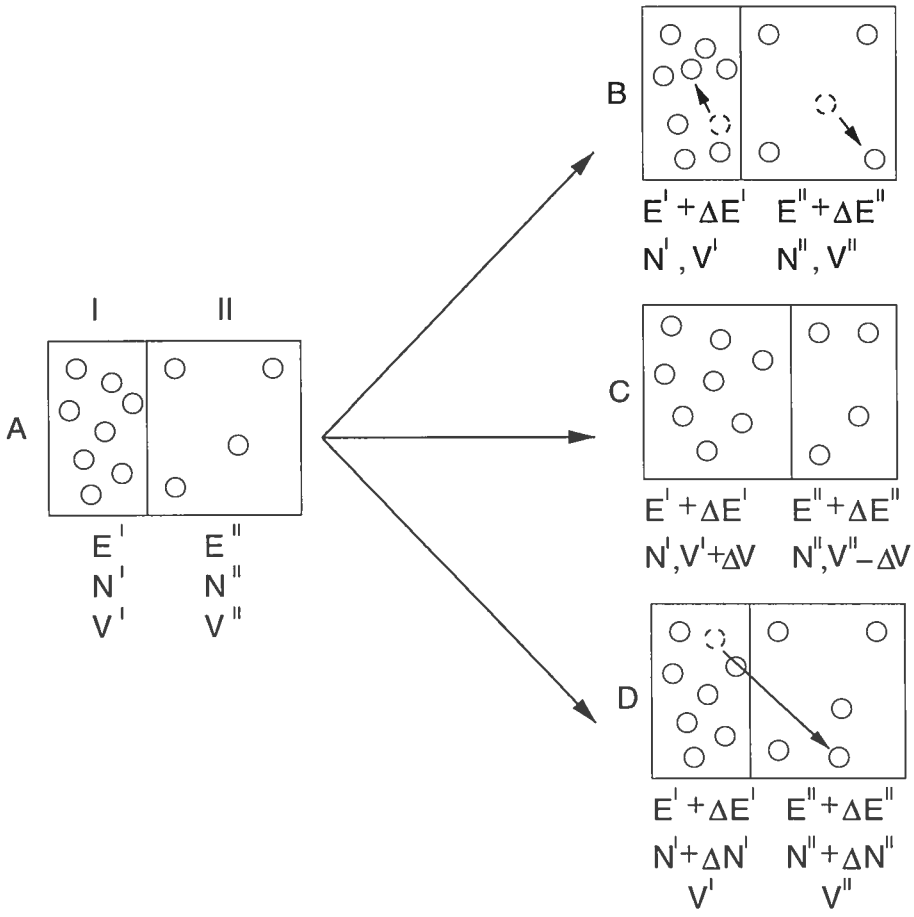

FIG. II.1 – Représentation schématique des mouvements possibles dans l'ensemble de Gibbs.

d'une particule à l'intérieur d'une boîte ($A \rightarrow B$), réarrangement du volume des deux boîtes ($A \rightarrow C$) et échange de particules entre les deux boîtes($A \rightarrow D$).

Décrivons maintenant les différents types de mouvement en détail.

II.1.1.1 Déplacement d'une particule

Lors de ce type de mouvements, les deux boîtes sont indépendantes. L'explication donnée ici pour la boîte I s'applique donc aussi à un mouvement à l'intérieur de la boîte II. Dans le cadre de ce mouvement, la boîte est un système tiré de l'ensemble canonique. Les états dans cet ensemble surviennent avec une probabilité proportionelle à $\exp(-\beta E^I)$ où E^I est l'énergie configurationnelle de la phase I. Lors d'un mouvement, une particule choisie au hasard se voit attribuée un dépla-

cement aléatoire qui l'amène à une nouvelle position d'essai. Cet essai est accepté avec une probabilité donnée par $\min(1, \mathcal{P}^I_{\text{depl}})$ avec

$$\mathcal{P}^I_{\text{depl}} = \exp(-\beta \Delta E^I) \tag{II.1}$$

où ΔE^I est le changement d'énergie configurationnelle dû à ce mouvement. Ce type de mouvement assure que la température de chaque boîte correspond bien à la température fixée. Si le mouvement est refusé, l'atomes est replacé à sa position initiale, i.e. un essai refusé est sans conséquence.

II.1.1.2 Réarrangement du volume

Dans le deuxième type de mouvements, les deux boîtes sont corrélées. Maintenant, chacune des deux boîtes fait partie d'un ensemble isobare-isotherme. Le mouvement d'essai consiste en un changement de volume ΔV pour la boîte I et donc d'un changement de volume $-\Delta V$ pour la boîte II (le volume total étant fixe). Le changement de volume entraîne une renormalisation des coordonnées de chaque atome et de la dimension des boîtes et donc un changement de leurs énergies potentielles ΔE^I et ΔE^{II}. Cet essai est accepté avec une probabilité donnée par $\min(1, \mathcal{P}^I_{\text{vol}})$ avec

$$\mathcal{P}^I_{\text{vol}} = \exp\left[-\beta\left(\Delta E^I + \Delta E^{II} - N^I \ln(\frac{V^I + \Delta V}{V^I}) - N^{II} \ln(\frac{V^{II} + \Delta V}{V^{II}})\right)\right] \tag{II.2}$$

Si le mouvement est refusé, les deux boîtes retournent dans leur configuration initiale. Ce type de mouvement est utilisé pour équilibrer la pression entre les deux compartiments.

II.1.1.3 Échange de particules

Finalement, des échanges de particules entre les deux boîtes sont permis dans le but d'égaliser le potentiel chimique des deux phases. Ce mouvement combine la création d'une particule dans une des boîtes avec la destruction d'une particule choisie au hasard dans l'autre boîte (voir mouvement $A \rightarrow D$ de la figure II.1). La boîte source et la boîte cible sont déterminées aléatoirement. Cet échange entraîne

un changement d'énergies configurationnelles ΔE^I et ΔE^{II}. L'essai est accepté avec une probabilité donnée par $\min(1, \mathcal{P}^I_{\text{ech}})$ avec

$$\mathcal{P}^I_{\text{ech}} = \exp\left\{-\beta\left[\Delta E^I + \Delta E^{II} - k_B T \ln\left(\frac{V^{II}(N^I+1)}{V^I N^{II}}\right)\right]\right\} \tag{II.3}$$

Cette dernière expression suppose que la particule est transférée de la boîte II vers la boîte I. Pour le mouvement inverse, il suffit d'interchanger les indices. Encore une fois, en cas de refus, la deux boîtes retournent vers leur configuration initiales, sans autre conséquence.

II.1.1.4 Déroulement d'une simulation typique

Comme mentionné plus haut, une simulation complète dans l'ensemble de Gibbs comporte 3 types de mouvements possibles. Le nombre relatif d'essais de chaque types n'est pas dicté par la théorie, mais affecte la vitesse d'atteinte de l'équilibre. Un cycle Monte Carlo typique comporte N essais de déplacement (N étant le nombre total de particules), deux ou trois essais de changement de volume et environ un essai d'échange par particule. Le nombre d'essais d'échange doit être augmenté dans le cas où une des deux phases devient très dense car la probabilité d'insertion d'une particule dans la phase dense est extrêmement faible et donc la convergence du potentiel chimique très lente. Les cycles sont répétés jusqu'à ce que l'énergie et la pression à l'intérieur de chaque boîte soit convergée, ce qui requiert typiquement quelques milliers de cycles.

À la fin d'une simulation comportant ces trois classes de mouvements, la température, la pression ainsi que le potentiel chimique sont égaux dans chacune des boîtes et donc les phases I et II ont atteint l'équilibre. Les densités ρ^I et ρ^{II} et la pression P finales sont enregistrées et les simulations sont répétées pour plusieurs valeurs de T jusqu'à ce que la courbe de coexistence voulue soit connue dans son entiereté.

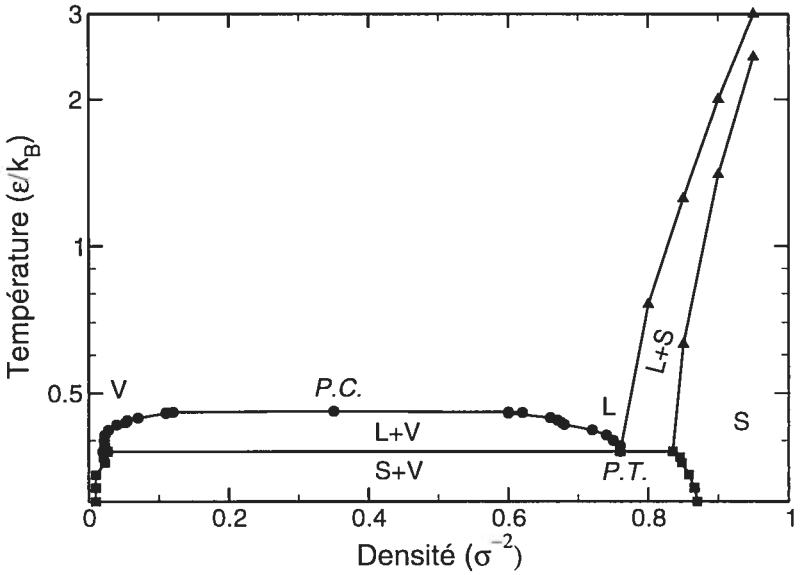

FIG. II.2 – Diagramme de phase du potentiel LJ 2D. Cercles : Courbe binodale, Carrés : Courbe de coexistence solide-vapeur, Triangles : Courbe de coexistence liquide-solide. Sigles : S →Solide, L →Liquide, G →Gas, $P.T.$ →Point triple et $P.C.$ →Point critique.

II.1.1.5 Résultats

Cette méthode a été appliquée au calcul de la binodale et de la courbe de coexistence solide-vapeur du potentiel LJ tronqué. Les résultats sont présentés à la figure II.2. Les valeurs obtenues en utilisant notre programme Monte Carlo sont compatibles avec les résultats publiés dans [47] pour la section à haute température de la binodale.

Une série de calculs DM dans l'ensemble micro-canonique a aussi été effectuée pour déterminer la surface d'équilibre du potentiel LJ dans le but de s'assurer que notre système soit en tout temps suffisamment près de l'équilibre local pour que l'utilisation de la thermodynamique soit justifiée lors de l'analyse des simulations d'ablation. La surface d'équilibre, présentée à la figure II.3, est aussi utilisée pour déterminer la dépendance en température de la résistance en tension (voir le second article pour les détails).

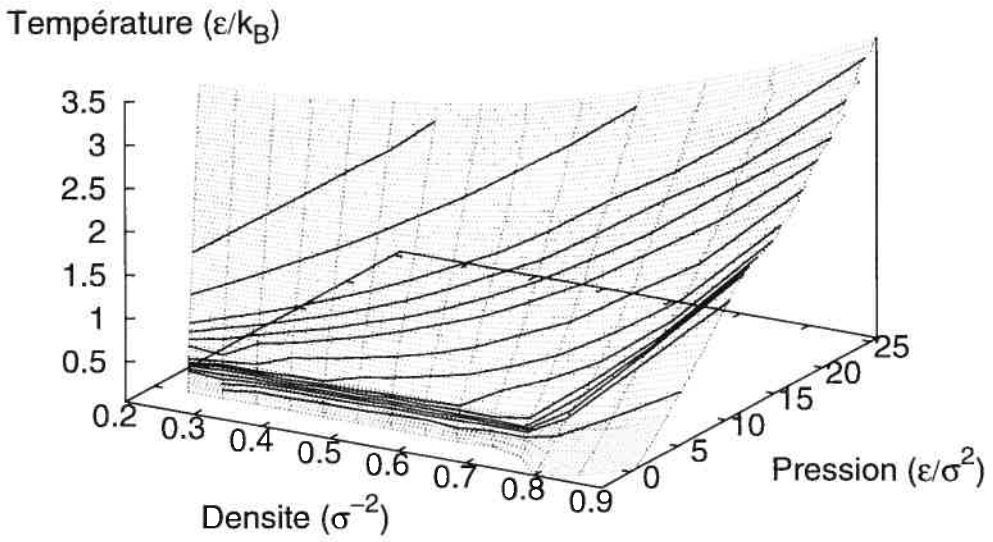

FIG. II.3 – Surface d'équilibre du potentiel LJ 2D. Lignes pleines : isentropes.

II.2 Entropie

Dans le but de déterminer si l'expansion de la cible lors de l'ablation s'effectue à entropie constante, nous avons aussi calculé l'entropie du système LJ pour un ensemble de densité et de températures différentes. Pour ce faire, la méthode proposée par [44] a été utilisée. L'entropie y est obtenue en considérant le système comme un ensemble d'oscillateurs harmoniques quantiques couplés. Dans ce formalisme, l'entropie est de la forme :

$$S = \frac{1}{2} k_B \ln \det[\mathbf{1} + \frac{k_B T e^2}{\hbar} \mathbf{M}\sigma] \tag{II.4}$$

où e est la constante d'Euler, $\mathbf{M} = m\mathbf{I}$ est la matrice diagonale contenant la masse des particules et σ est la matrice covariante de la fluctuation des positions atomiques telle que :

$$\sigma_{ij} = \langle (x_i - \langle x_i \rangle)(x_j - \langle x_j \rangle) \rangle \tag{II.5}$$

Cette méthode a été choisie car elle a déjà été appliquée avec succès au calcul de l'entropie du fluide LJ en trois dimensions.

Quelques isentropes ainsi obtenues sont présentées sur la surface d'équilibre de la figure II.3. Bien que l'approximation harmonique soit douteuse dans le cas d'un gas dilué, les isentropes obtenues répondent bien à la loi de Sakur-Tetrode (valide pour les gas parfaits) dans la région de faible densité et de haute température, ce qui renforce notre confiance dans les résultats. Puisque l'entropie varie brusquement lors d'un changement de phase, il a aussi été possible de délimiter grossièrement la position de la zone de coexitence liquide-solide (dans ce cas, les deux phases sont trop denses pour pouvoir utiliser le Monte Carlo dans l'ensemble de Gibbs). Les résultats sont présentés sur le diagramme de phase de la figure II.2 et complètent les données thermodynamiques requises pour l'analyse des résultats.